School of Chemistry

Fabrication of Black Diamond for Electrochemical Applications

Thomas Taylor

This thesis is submitted in partial fulfilment of the requirements for the Honours Degree of MSci (Bsc) at the University of Bristol

Supervisor – Paul May
Second Assessor- David Fermin
08/04/2023

Contents

Abstract

The aim of this project is to deposit highly conducting B-doped diamond (BDD) films upon nanostructured bSi substrates for use as high surface area electrodes. Diamond represents an attractive material for electrochemical applications due to its chemical inertness and mechanical hardness. By depositing thin films of B-doped diamond upon a substrate using chemical vapour deposition (CVD) the conductivity of diamond can be varied from insulating to near metallic, by changing the concentration of B-containing gas in the CVD gas mixture. This makes diamond even more attractive for electrochemical applications.

Black silicon (bSi) is a synthetic material which contains nanostructured spikes and needles on its surface. bSi is insulating, however, by depositing BDD films upon a bSi substrate, highly conductive, high surface area electrodes can be made.

In this work, BDD bSi electrodes were synthesised, using a nanodiamond seeding process before BDD film deposition in a hot filament CVD (HFCVD) reactor. The seeding conditions were varied to optimise the growth of diamond along the length of the bSi needles, as well as to avoid growth of diamond on top of the needles, rather than in between them (Fig.37). The diamond was initially H-terminated. Flat BDD electrodes were also synthesised.

Electrodes were produced using silver paint to connect a wire to the BDD side of the electrode, with Teflon tape used to secure a 3mm diameter area which would be used as the geometrical surface area of the electrode. Various electrochemical measurements were undertaken, including capacitance measurements in 100mM KNO_3 (Figs. 44, 45, 45a) and CV measurements in 1mM $K_3[Fe(CN)_6]$ with 100mM KCl at a variety of scan rates (Figs.46, 46a, 46b). Graphite and Ag/AgCl (3M KCl) were used as the counter and reference electrodes respectively.

Two bDi electrodes were tested (MM15 and MM17), with each having a different level of BDD growth along their surface (Figs. 40-43). Capacitance values (Table 10) of 59.7 μF cm^{-2} and 44.8 μF cm^{-2} were obtained for MM15 and MM17 respectively. The electrodes were subjected to ozone treatment to O-terminate the diamond, as this creates a hydrophilic surface compared to the hydrophobic H-terminated diamond. Capacitance experiments were then repeated (Table 12), with values of 828.0 μF cm^{-2} and 84.7 μF cm^{-2} obtained for MM15 and MM17 respectively. Both MM15 and MM17 were found to have a surface area ~12 times larger than a flat electrode.

Similar data collected by May *et al.*[30] (Table 1) suggests that capacitance is proportional to bSi needle length. The surface area and MM17 capacitance values are concurrent with this data. However, the MM15 capacitance is much larger than the longest bSi needle length used by May *et al.* This suggests that the major disparity in capacitance values between MM15 and MM17 is due to either leakage of electrolyte solution to areas outside the defined geometrical area of the electrode in MM15, or differences in the amount of BDD diamond deposition. Repeatability measurements need to be undertaken to confirm this but were not completed in time.

Nonetheless, the data collected shows that nanostructured BDD electrodes have higher capacitance and surface area values than conventional flat diamond electrodes. Previous research has shown applications of these electrodes in highly sensitive hormone detection[25, 30, 33], as well as water treatment[37].

Literature Review - Microstructured Diamond for Electrochemistry

Introduction

Electrochemistry

Electrochemistry involves the study of oxidation and reduction reactions at polarised electrode surfaces.[1] Each analyte is oxidized or reduced at a specific potential. If an electron transfer between two molecules in aqueous solution is thermodynamically favourable, a reaction will occur.[1]

There are three electrodes in a typical setup: a working, reference and counter electrode. Electron transfer occurs at the working and counter electrodes, with current carried through the solution by the diffusion of ions created at each electrode. A capacitive electrical double layer is formed at each electrode during this process, known as the diffuse double layer (DDL). The reference electrode provides a stable and well-known potential. Fig.1 shows an example electrochemical setup.

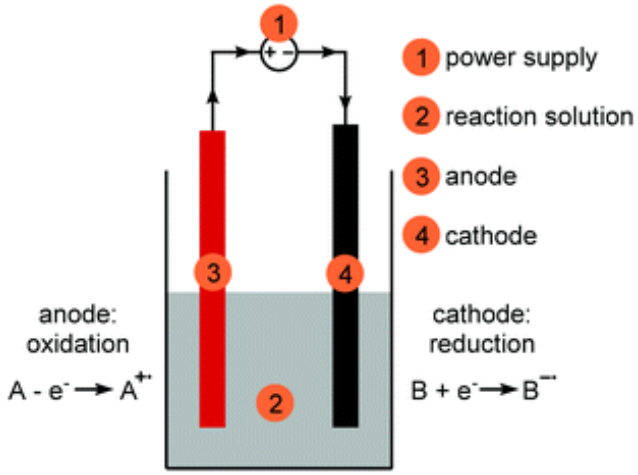

Fig.1 - Example of simple electrochemical setup. Taken from Ref.002

The type of heterogeneous reaction that takes places at the DDL can be one of two types.[3] The first is called outer-sphere electron transfer. No new bonds are broken or formed, and this mechanism can occur between species that are identical except for their oxidation state.[4] The transfer of electrons between the electroactive species and the electrode takes place by tunnelling across a monolayer of solvent attracted to the electrode.[3] The rate is determined by the orientation of the solvent molecules.[3] A widely used outer-sphere electron transfer mechanism is the ferri/ferrocyanide ($[Fe(CN)_6]^{3-/4-}$) redox couple, which is used in the experimental section of this work.

Inner sphere electron transfer is the other reaction type. Bonds are broken and formed, and the electron transfer takes place through a bridging ligand between the oxidised and the reduced species.[4] The identity of the electrode plays a vital role. The reactant, product, and/or intermediate species are strongly bound to the electrode through which electron transfer can occur between the electrode and the electroactive substance in solution.[3] The rate may be increased by changing the electrode and/or electrolyte, or by modifying the electrode surface.[3] Fig.2 shows a representation of outer- and inner-sphere electron transfer.

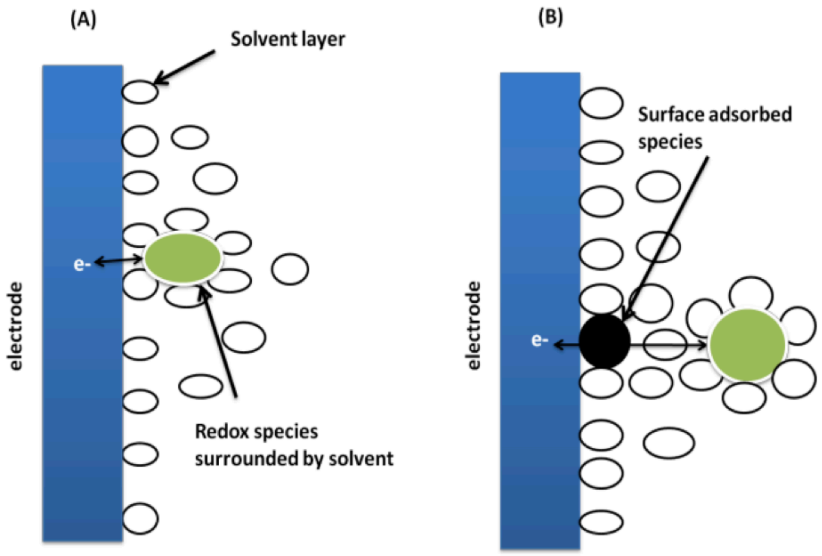

Fig.2 - Illustration of (A) outer-sphere electron transfer and (B) inner-sphere electron transfer. Taken from Ref.003.

Cyclic voltammetry (CV) is a type of electrochemical measurement. The electrode potential is ramped linearly versus time, before being ramped in the opposite direction to return to the initial potential.[5] Cyclic voltammograms (CVs) are plotted as the current at the working electrode against the applied voltage. CVs are 'duck-shaped' plots.[5] Fig.3 shows an example CV.

Initially, the voltage is not high enough to oxidise the analyte (a). As the applied potential increases, the onset of oxidation (E_{onset}) is reached. The current then exponentially increases (b) as the analyte begins oxidation at the working electrode surface. As the current rises, the amount of oxidant decreases and the concentration gradient decreases, before reaching a peak (c). The peak is known as the anodic peak current (i_{pa}) for oxidation at the anodic peak potential (E_{pa}).[5]

The current then decreases (d) until a steady state is reached; further increases in potential no longer affect the reaction. The potential then reverses to negative potentials which continues to oxidise the analyte until the applied potential reaches the point where re-reduction of the analyte can occur (e). The cathodic peak (i_{pc}) and cathodic peak potential (E_{pc}) (f) mirror that of oxidation.[5] The area inside a cyclic voltammogram is proportional to the surface area of the working electrode.[6]

The peak current, i_p, can be calculated using the Randles-Sevcik equation.[5] At 298K:

$$i_p = (2.69 \times 10^5) n^{3/2} A C D^{1/2} v^{1/2} \qquad (1)$$

n is the number of electrons, A is the electrode area (cm^2), C is the concentration (mol cm^{-3}), D is the diffusion constant (cm^2 s^{-1}), and v is the potential scan rate (V s^{-1})[5].

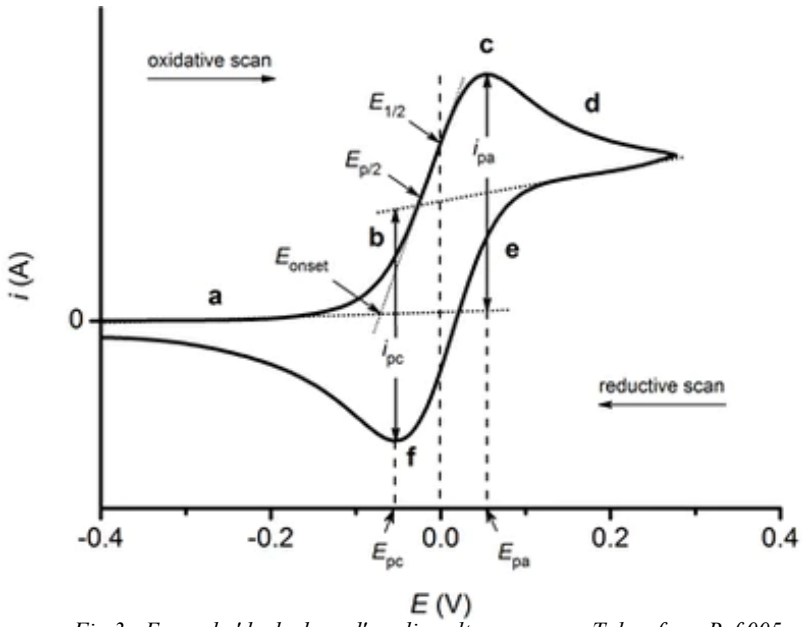

Fig.3 - Example 'duck-shaped' cyclic voltammogram. Taken from Ref.005.

Another voltammetry technique mentioned later in this review is differential pulse voltammetry (DPV). Unlike in CV, where the electrode potential is ramped linearly versus time, before being reversed, the potential in DPV is applied in low amplitude, short pulses on a linear ramp increase.[7] The current is measured before and after each pulse before the difference is calculated. This effectively reduces background current and leads to high sensitivity. Because of this advantage, DPV has been used for high precision detection of hormones, seen later. Fig.4 shows an example voltammogram produced from DPV.[7]

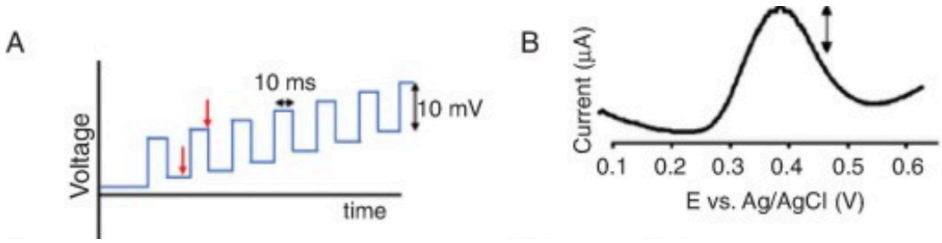

Fig.4 - (A) Applied potential for DPV. Red arrows show points where current is measured. (B) DPV voltammogram. Taken from Ref.007.

Carbon as an Attractive Electrode Material

Electrode materials should be highly conductive, have good mechanical properties as well as strong chemical resistance. For scaled up applications, they need to be produced at a low cost.[8] Fig.5 summarises the characteristics of an ideal electrode.

Carbon is a useful material for electrochemical applications due to its various allotropes (graphite, diamond, and nanotubes), existence in different forms, and its various microstructures (more or less ordered).[10] Carbon is chemically stable in different solutions and performs at a wide range of temperatures. Carbon electrodes are easily polarised; however, their conductivity depends largely on the hybridisation and content of heteroatoms. Doping the carbon structure with nitrogen[11], boron[6] and nickel[12] have all been shown to significantly increase the conductivity of carbon.

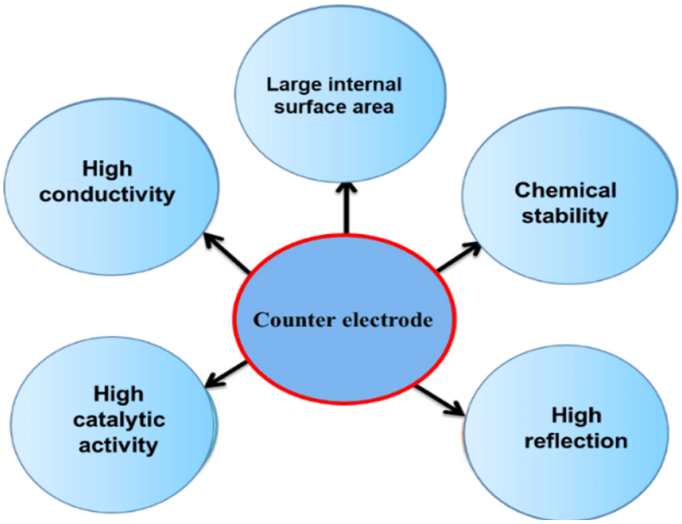

Fig.5 - Characteristics of an ideal electrode. Taken from Ref.009.

In addition to this, carbon electrodes are easily accessible, easily processed and relatively low cost. They are also environmentally friendly.[10] All of these characteristics make carbon a very attractive material for electrochemistry.

Chemical Vapour Deposition (CVD)

Chemical Vapor Deposition (CVD) is a process in which a solid substrate is exposed to a volatile precursor molecule. This reacts on the substrate surface, which over time produces a desired thin film.[13]

CVD diamond films have had significant scientific interest over the last few decades due to their mechanical hardness, conductivity and optical transparency.[6] Producing these films requires a carbon precursor gas (usually methane) diluted with hydrogen (1% vol CH_4), which causes deposition onto the substrate. Figs.6 and 7 show schematic examples of diamond CVD reactors.

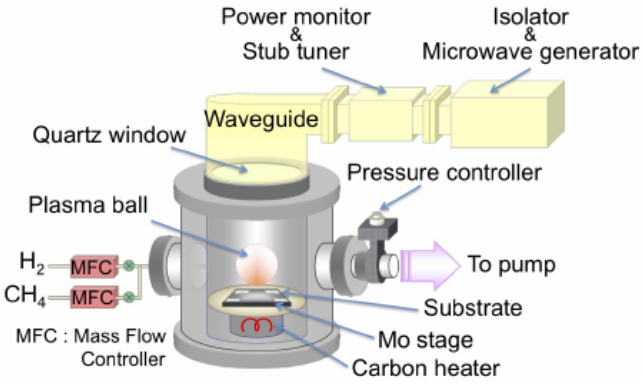

Fig.6 – Schematic of microwave plasma-enhanced CVD system used for the growth of diamond. Taken from Ref.014.

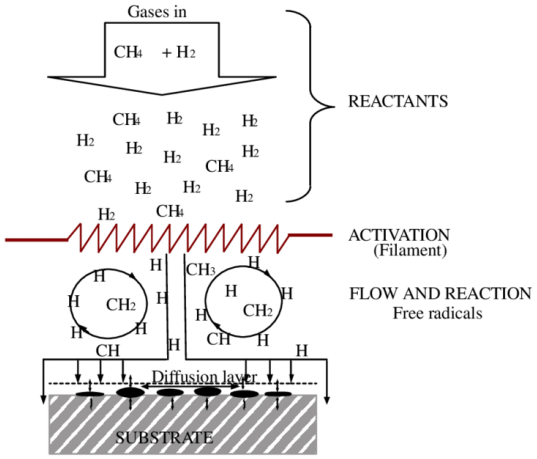

Fig.7 - Schematic diagram of diamond CVD process. Taken from Ref.015.

A temperature of more than 700°C is needed to ensure diamond growth as opposed to amorphous carbon.[16] Whilst diamond itself is insulating, the CVD process can be altered to dope the diamond film and vary the conductivity, making it an attractive material for electrochemical applications.[6,11,12]

Microporous Carbon Electrodes

Boron-Doped Diamond

Most semiconductors are formed by replacing atoms in a host crystal with elements which have either more or less valence electrons.[17] This is called doping. Elements with more valence electrons than the atoms in the host crystal are called donors and give rise to n-type semiconductors. Elements with fewer valence electrons are called acceptors and give rise to p-type semiconductors.[17]

For conduction to occur, electrons must be promoted from the valence band into the conduction band. The energy difference between the highest occupied state of the valence band and the lowest unoccupied state of the conduction band is called the band gap. The size of the band gap is indicative of the electrical conductivity of a material.[18] If the band gap is large, a lot of energy is required to promote the valence electrons into the conduction band. Similarly, if there is no band gap, as in metals, the electrons can freely move between the two bands and the material is highly conductive.[18] Fig.8 shows a representation of this.

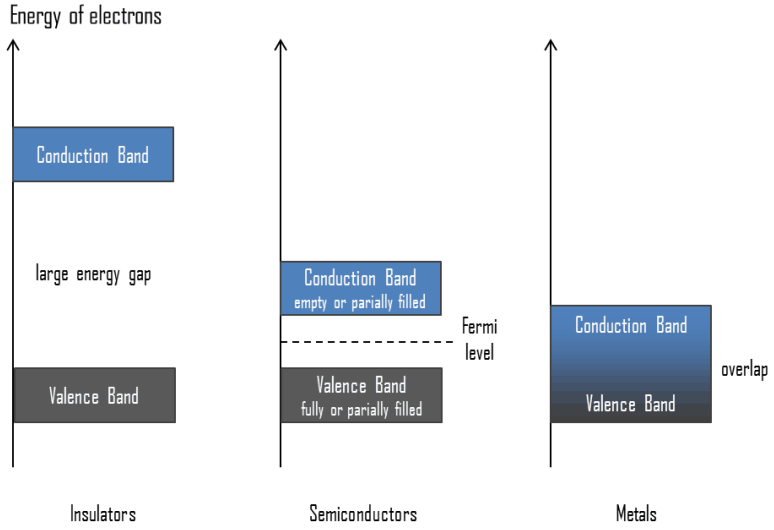

Fig.8 - Representation of conduction and valence bands in insulators, semiconductors, and metals. The Fermi level is the highest occupied electron energy level at absolute zero. Taken from Ref.019.

Based on these principles, diamond can be doped with either boron or nitrogen, corresponding to the two elements alongside carbon in the periodic table. However, nitrogen is essentially useless as the donor level sits deep below the conduction band with an energy difference of 1.7eV at room temperature.[20]

Boron, however, is a successful dopant within diamond. It is a p-type dopant, with its valence band at around 0.37eV above the diamond valence band maximum.[20] Zanin *et al*.[6] have described a process whereby the CVD diamond film process can be altered to dope the film with boron. Adding a boron-

containing gas into the CVD gas mixture during diamond growth allows doping to be achieved. By varying the concentration of the boron-containing gas, the conductivity of the diamond film can be tuned, from insulating to near-metallic.[6]

The experimental procedure followed by Zanin *et al*.[6] involved a short (1.5h) diamond CVD process in a hot filament reactor using 1% CH_4/H_2 with diborane (B_2H_6) as the boron containing gas. Two different types of vertically aligned carbon nanotube (VACNT) structures with varying porosity were used to deposit the boron-doped diamond (BDD) CVD film.

The first involved growing multiwalled carbon nanotubes (MWCNTs) in a plasma enhanced CVD reactor on a Si substrate. A VACNT forest was produced (carbon nanotubes (CNTs) length: ~5μm, width: 20−50 nm, density: $\sim 1 \times 10^9$ cm^{-2}). The VACNT forest was then electrospray seeded with a nanodiamond seed solution (5 nm nanodiamond in methanol), which caused the tops of the CNTs to join together into teepee-like structures. Each teepee consisted of ~20−40 CNTs joined at the top (teepee density: $\sim 10^7$ cm^{-2}). The teepees were coated with a thin layer of BDD, (thickness ~0.5 μm). The B_2H_6 concentration in the CVD gas-mixture was high enough to ensure conductivity of the BDD film was near metallic.[6]

The second VACNT forest was produced (CNT length: 40 μm, density: $\sim 2.5 \times 10^{10}$ cm^{-2}). The substrate was also changed, from poorly conducting Si to a conducting Ti substrate. Instead of forming teepees, the higher packing density led to long extended ridges or honeycomb-like structures being formed. The BDD CVD film was then deposited under the same conditions as the first structure.[6]

As a control sample, a flat BDD film was deposited onto a flat silicon substrate (thickness: ~1−2 μm). The structures of each sample were observed using scanning electron microscopy (SEM), seen in Fig.9.

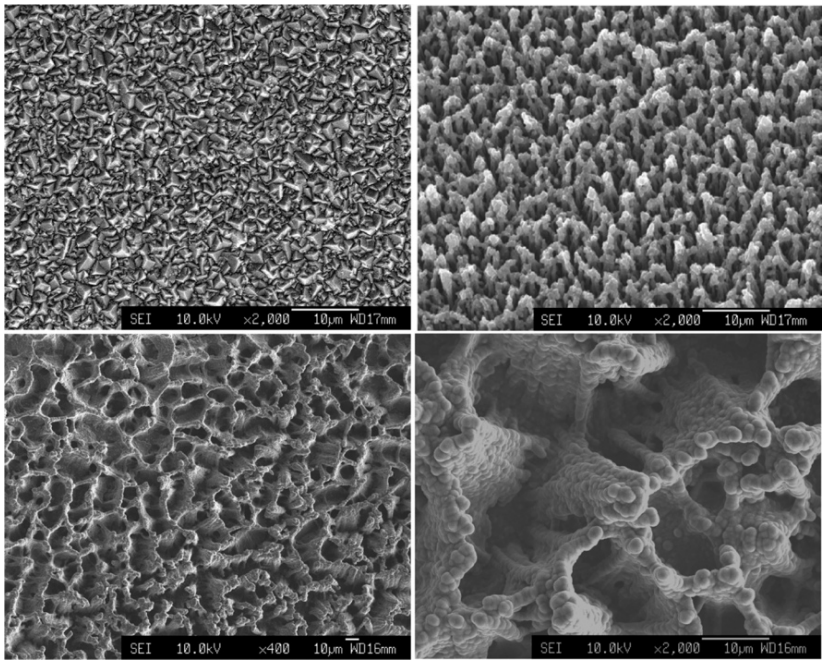

Fig.9 – SEM images of (a) Flat control sample, (b) Teepee structure, (c) Honeycomb structure, (d) Enlarged image of (c). Taken from Ref.006.

Fig.10 shows various CVs from the nanostructured BDD electrodes in different electrolyte solutions. Fig.10a shows capacitance CVs in a 0.1M KNO_3 electrolyte solution. Capacitance is a measure of how well a material can hold electrical charge. These CVs are quasi-rectangular in shape which is

indicative of double-layer charging.[21,22] The larger the area within the CV, the higher the capacitance of the electrode.

Figs.10b and 10c show 'duck-shaped' CVs in two different electrolyte solutions. Looking at the area within these CVs, the honeycomb sample has the highest capacitance and the highest electroactive surface area. This could be due to the longer carbon nanotubes used to form the VACNT forest.[23] The CV from the flat BDD electrode has negligible area, indicating a significantly lower electroactive surface area compared to the teepee and honeycomb structures.[23]

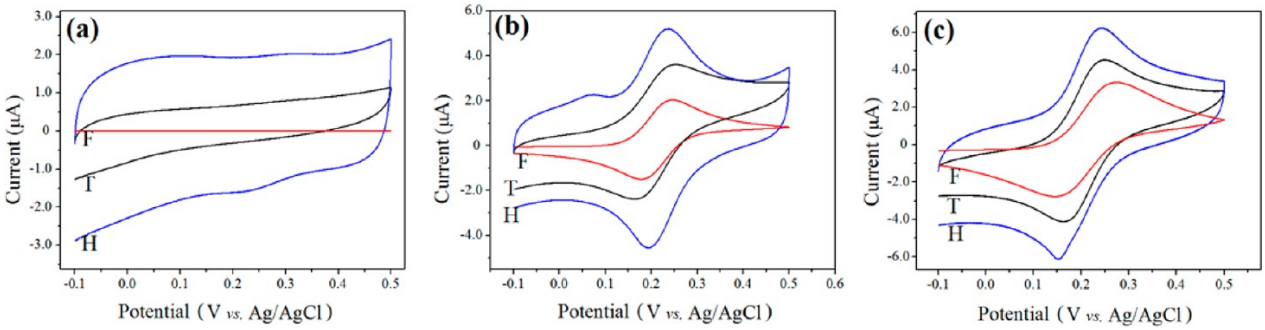

Fig.10 - CV plots of electrodes in (a) 0.1M KNO_3, (b) 0.5nM ferrocene-methanol in 0.1M KNO_3 and (c) 1mM ferri/ferrocyanide in 0.1M KNO_3. Flat (F), teepee (T) and honeycomb (H). Taken from Ref.006.

Zanin *et al*.[6] found that the electroactive surface area of the nanostructured electrodes was 450 times greater than the flat electrode. The capacitance values for the nanostructured electrodes were 150−450 times greater than for the flat electrode, indicating their greater ability to store electrical charge.[6]

The conclusions of this work suggest a multitude of applications are possible using these electrodes. By combining the high conductivity and surface area of CNTs with the robust and inert surface of diamond, highly sensitive electrodes can be fabricated.[6] Possible applications as biosensors are suggested. Biosensors transduce biochemical events into electrical signals.[24] The huge surface area of these electrodes should improve a biosensors ability to detect trace amounts of redox species, improving accuracy.[6]

Diamond-like Carbon (DLC) Electrodes

Diamond-like carbon (DLC) is an amorphous form of carbon that contains both tetrahedral (sp^3) and trigonal (sp^2) hybridisations, which can be deposited in various amounts depending on the reaction conditions.[25] The properties of DLC are like crystalline diamond (chemical inertness, hardness, and optical transparency), hence making DLC an attractive material as a protective coating. DLC films are electrically insulating, preventing their use in electrochemistry. Similarly to the BDD CVD films[6], attempts have been made to incorporate n- and p-type dopants to improve conductivity, however, the focus of the research by Zanin *et al*.[26] was to avoid doping. Instead, they concluded a better option may be to incorporate conductive forms of carbon, such as CNTs, into the DLC.[26]

Their previous work has seen MWCNTs incorporated into the structure[27], as well as VACNTs.[28] VACNT films were prepared using microwave plasma CVD (MPCVD) on a Ti and Ni substrate, before a DLC film was deposited upon them using plasma enhanced CVD (PECVD). A flat control DLC electrode was deposited onto a Si wafer substrate. A web-like DLC:VACNT structure was produced, shown in Fig.11.

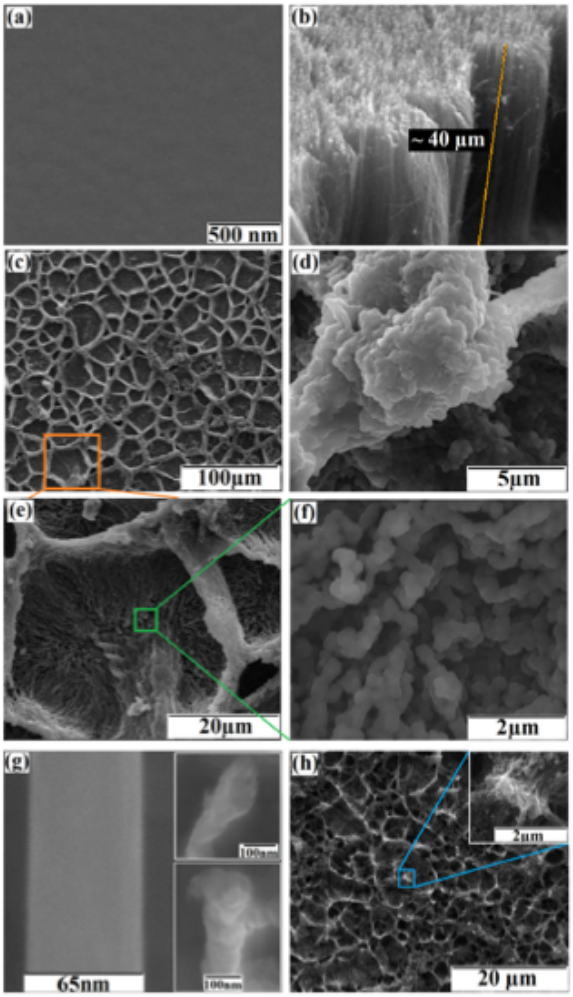

Fig.11 – (a) DLC Si film, (b) VACNT forests, (c) DLC:VACNT surface with web-like structure, (d - f) Magnification of the ridges and valleys seen in the DLC;VACNT sample, (g) Enlargement of a single CNT and (h) VACNT sample which has been wetted with water, showing formation of microstructures. Taken from Ref.026.

Following formation, the Raman spectra of the DLC films were measured, shown in Fig.12.

The spectrum of the DLC:Si film (Fig.12b) has two broad bands centred at 1340 cm^{-1} (D-band) and 1537 cm^{-1} (G-band). These arise from the breathing and stretching vibrational modes of sp^2 carbon sites, respectively.

The spectrum of the pure VACNT arrays (Fig.12c) has two distinct bands at 1357 cm^{-1} (D-band) and 1585 cm^{-1} (G-band). The D-band arises from defects and disordered carbon, whilst the G-band arises from well-ordered crystalline graphite.

The spectrum of the DLC:VACNT sample (Fig.12d) appears as a combination of the DLC and VACNT Raman characteristics. This suggests that the strength and integrity of the VACNT film is unaffected by coating with the DLC film.[26]

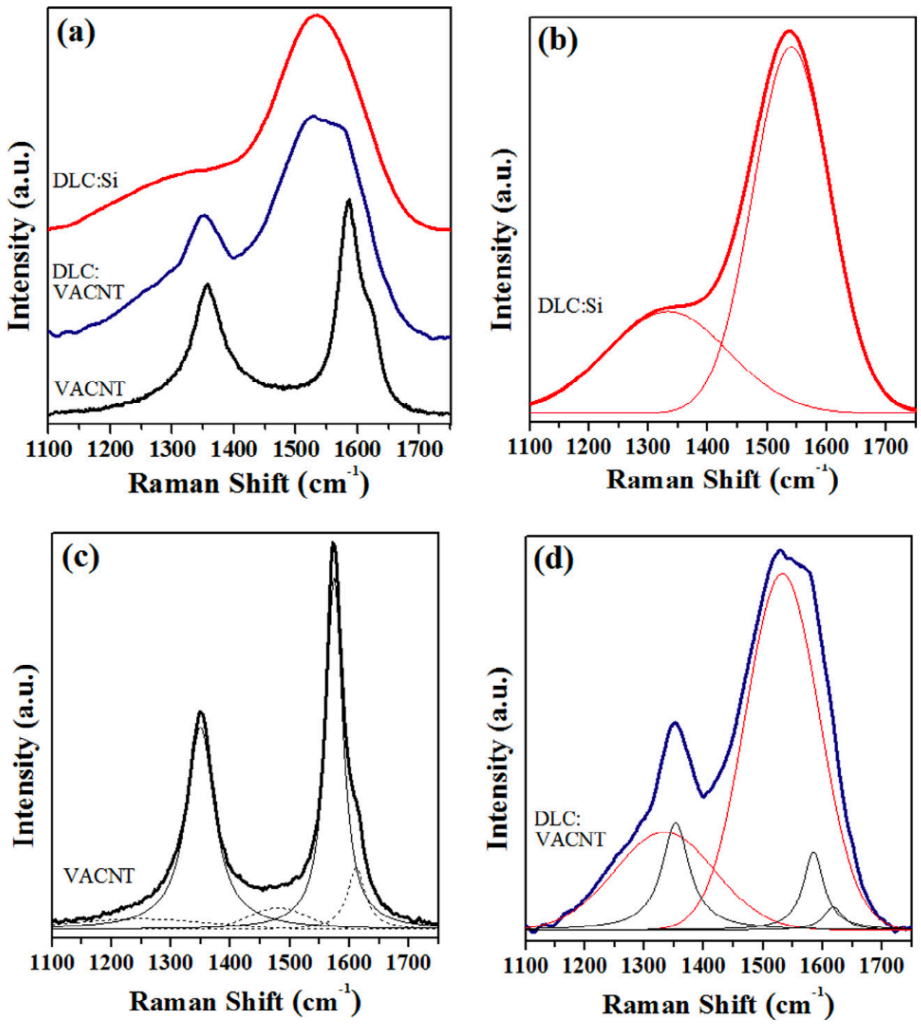

Fig.12 - Raman spectra of the (a) DLC:Si, VACNT and DLC:VACNT composites, (b) DLC:Si film, (c) VACNT and d) DLC:VACNT. Taken from Ref.026.

Capacitance CVs were produced (scan rate:100mVs^{-1}, electrolyte solution: 0.1M KNO_3), shown in Fig.13. The CVs from all electrodes (Fig.13a) show a remarkable contrast between the conductivity of the DLC films on Si to those on VACNTs. The flat DLC:Si is effectively highly insulating, shown by the negligible surface area within the capacitance CV.

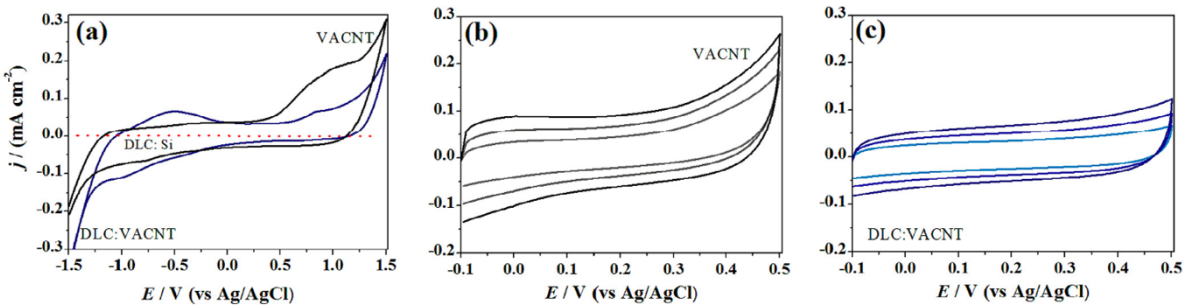

Fig.13 – (a) Cyclic voltammetry measurements of each electrode, (b) VACNT and (c) DLC:VACNT. Taken from Ref.026.

For the VACNT (Fig.13b) and DLC:VACNT (Fig.13c) electrodes, as the potential scan rate increases, the capacitive current increases linearly, leading to capacitance values of 875 µF cm^{-2} and 642 µF cm^{-2} respectively.

Typical double-layer capacitance values for flat carbon electrodes are ~ 5 µF cm^{-2}. This suggests that the roughness factor (electrochemical surface area divided by the geometrical area[29]) associated with the DLC:VACNT electrode is around 130. This result suggests that adding a DLC coating to the VACNT array leads to a 32 ± 4% decrease in the electroactive surface area.[26]

The electrochemical responses (Fig.13) provide evidence that the films are conductive over the whole surface. However, due to the complex nanostructures of the VACNTs, electron transfer is potentially only taking place where the CNTs are exposed to the electrolyte. To test whether this is the case, conductance mapping of the DLC:VACNT film was undertaken using conducting atomic force microscopy (AFM). A 30 µm line scan measured the height (z) of the ridge from its peak (z = 19 µm) to the valley bottom (z = 0 µm), shown in Fig.14.[26]

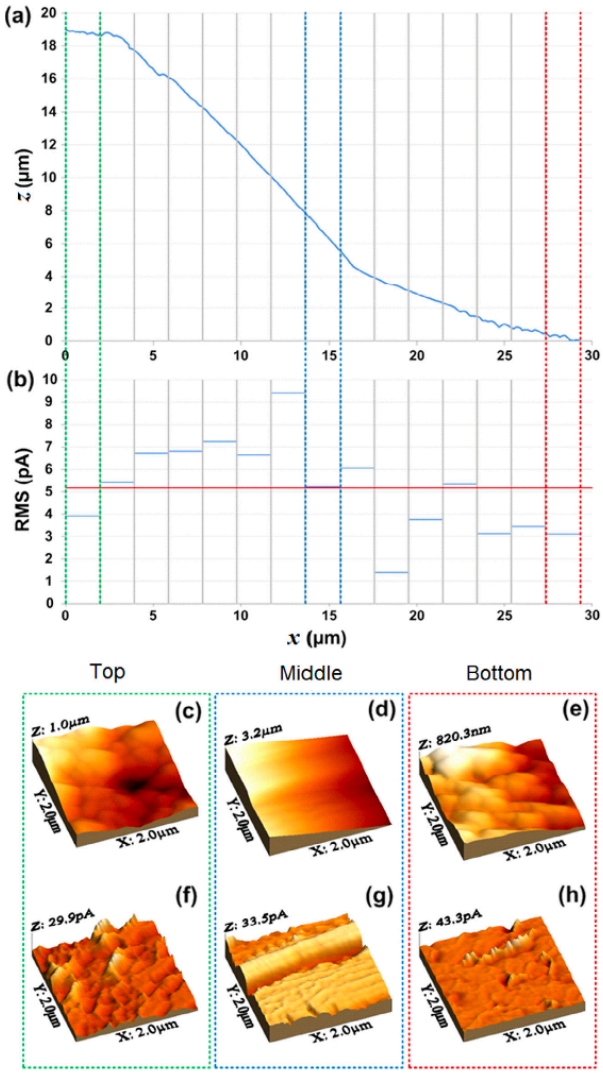

Fig.14 – Atomic force microscopy (AFM) measurements of the current and surface features within a 2 × 30 µm scan region. The scans begin at the base of ridge, extending to the top in a DLC;VACNT film. (a) Surface features along the central line of each 2 × 2 µm scan, which have been combined to make one continuous scan. This is displayed as vertical height, z, over a height of 19 µm. (b) Root mean square (RMS) of the current measured across each 2 × 2 µm scan. The red line at 5.2pA is the average current measured across the 2 × 30 µm region. An average RMS error of 39% was calculated. (c-h) Surface features of a series of 2µm × 2µm regions as well as the AFM current maps for the top, middle and bottom of the ridges. Taken from Ref.025.

Top of ridge (green: (0–2 μm)), middle of ridge (blue: (13–15 μm)) and bottom of ridge (red: (28–30 μm)). The RMS at the top of the ridges is very similar to the valleys of the film, meaning measured current and film conductivity are independent of surface features.

There is no clear correlation of conductance with larger surface features. This suggests that the conductivity of the DLC:VACNT films is connected to areas of high electron density, as opposed to parts of the CNT support which are directly exposed to the electrolyte solution.[26]

Diamond-Coated Black Silicon

Black silicon (bSi) is a synthetic material which contains nanostructured spikes and needles on its surface.[30] A plasma etching technique is used to produce these. May *et al*.[30] have showed that by coating a bSi surface uniformly with a BDD film, robust, sensitive, and high surface area electrodes can be produced. A ferri/ferrocyanide outer-sphere electron transfer probe was used to assess the electrochemical responses.

Two bSi substrates were produced, one containing short needles (length: ~ 1 μm) and the other with long needles (~ 15-20 μm). The samples were then electrospray seeded with a nanodiamond seed solution (5 nm nanodiamond in methanol), The electrostatic attraction between the substrate and the suspension caused the bSi needles to be covered completely with a near monolayer of ~10nm nanodiamond seeds, even on the vertical sides of the needles.

The samples were then placed in a hot filament CVD reactor (HFCVD) and films (thickness: ~ 0.25 μm) of either (i) heavily boron-doped microcrystalline diamond (MCD) or (ii) heavily boron-doped nanocrystalline diamond (NCD) was deposited. Doping in both samples was sufficient to ensure near metallic conductivity. Fig.15 shows the resulting samples. The substrates were immobilised on a copper plate to ensure use as a working electrode.

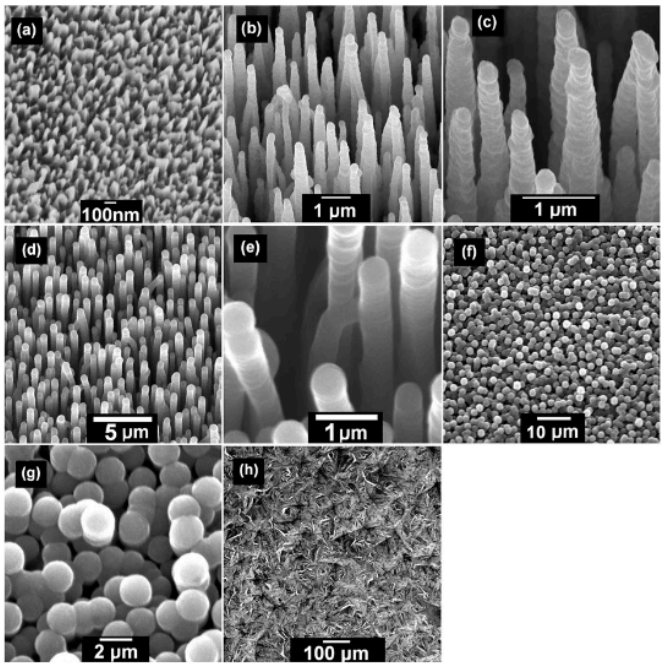

Fig.15 – (a) Short needles, (b and c) Long needles coated with MCD, (d and e) Long needles coated with NCD, (f and g) Slightly overgrown long needles with NCD with cavities allowing access to the interior of film, (h) Commercial flat BDD electrode. Taken from Ref.030.

Table 1 shows the capacitance and relative electroactive surface area measurements for each electrode.[30]

Table 1 - Capacitance and effective electroactive surface areas relative to flat BDD electrode. Taken from Ref.030.

Electrode	Capacitance/ ($\mu F\ cm^{-2}$)	Relative effective surface area
Flat BDD (Element Six)	2.9	1.0
BDD-coated bSi short needles	7.6	2.6
BDD-coated bSi long needles	279.4	97
Partially overgrown BDD-coated bSi long needles	638.0	221

Capacitance values of ~ 280 $\mu F\ cm^{-2}$ for the BDD-coated long bSi needles and ~ 640 $\mu F\ cm^{-2}$ for the partially overgrown needles were calculated. These capacitance values are particularly high compared to ~ 5 $\mu F\ cm^{-2}$ for flat carbon electrodes, making these electrodes candidates for supercapacitor applications. Capacitance is seen to be a function of the bSi needle length, meaning the capacitance of the electrode can be varied by changing the etch time used to create the substrate.[30]

Nickel-Decorated BDD Electrodes

Electrocatalytic materials are the focus of many research areas, including fuel cell catalysts and electrochemical sensors.[31] Nickel hydroxide ($Ni(OH)_2$) is one of the promising candidates, with the electrocatalytic effect thought to arise from unpaired d-electrons or empty d-orbitals in oxidised Ni, which are available for bond formation.[31] Decorating supporting substrates with nanoparticles has been found to significantly improve catalytic activity over bulk structures.[32]

L.Hutton *et al*.[31] precipitated randomly isolated $Ni(OH)_2$ nanoparticles on a hydrophilic O-terminated CVD BDD surface. To do this, a base was electrochemically generated in the presence of Ni^{2+} ions, to form a supersaturated nickel hydroxide solution. A 10mM Ni(NO solution (pH = 6) was used, with Pt as the counter electrode and Ag/AgCl as the reference electrode. The precipitation is thought to occur due to the electroreduction of nitrate ions in solution.[31]

$$NO_3^- + 7H_2O + 8e^- \rightarrow NH_4 + 10OH^- \quad (2)$$

This causes an increase in pH, which drives precipitation of solid $Ni(OH)_2$ on the BDD surface.

$$Ni^{2+}(aq) + 2OH^-(aq) \rightarrow Ni(OH)_2\ (s) \quad (3)$$

To drive the homogenous nucleation of $Ni(OH)_2$ nanoparticles in solution, it is important to:

I. Produce a high concentration of OH^- ions.
II. Avoid nanoparticle build-up by keeping the process short.

Different combinations of time and electrode potential were tried to find the optimal deposition conditions. A potential of - 1.1 V vs Ag/AgCl for 1 to 100s was found to be the most effective strategy. The reaction was done in situ with a BDD surface, causing nanoparticle precipitation to occur.[31] Fig.16 shows SEM images of the $Ni(OH)_2$ nanoparticles deposited on the BDD electrode surface. After 30s, some aggregation can be seen in the inset of Fig.16b, with much more aggregation after 100s in Fig.16c. Mean size of the nanoparticles was shown to increase with deposition time.

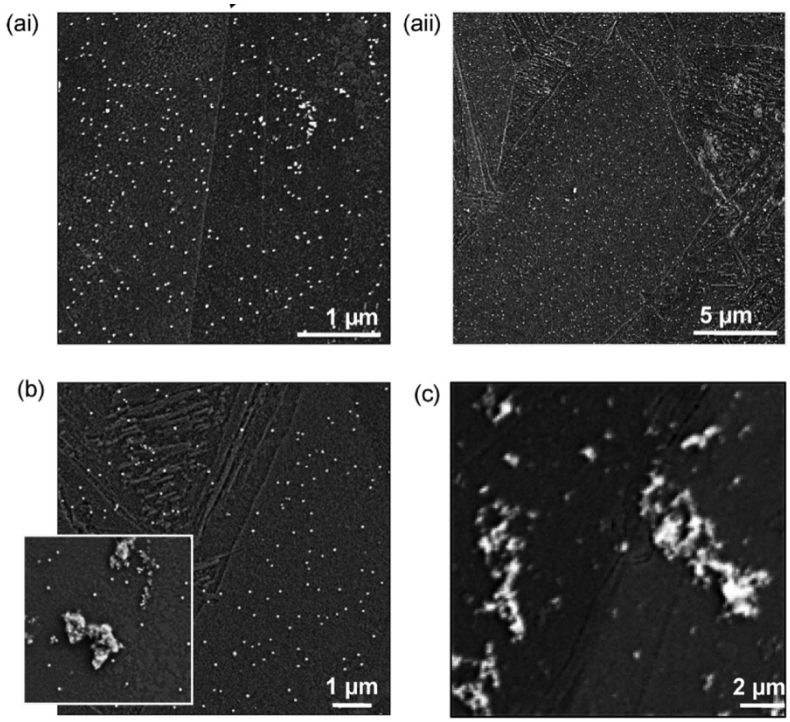

Fig.16 - $Ni(OH)_2$ deposited on BDD electrodes (ai) $\Gamma \sim 20$ nmol cm^{-2}, (aii) higher resolution of (ai), (b) $\Gamma \sim 140$ nmol cm^{-2}, (c) $\Gamma \sim 420$ nmol cm^{-2}. Deposition times at -1.1V vs Ag/AgCl were 5, 30 and 100s respectively. Taken from Ref.031.

Simple CV measurements were undertaken to estimate the amount of electroactive $Ni(OH)_2$ on the electrode surface. Fig.17 shows a typical CV recorded in 0.1M KOH for $\Gamma \sim 20$ nmol cm^{-2} $Ni(OH)_2$ (where Γ is the effective surface concentration of $Ni(OH)_2$ on the BDD electrode surface) after 5s deposition time. The current increases as the potential increases because of oxidation of Ni^{2+} to Ni^{3+}.

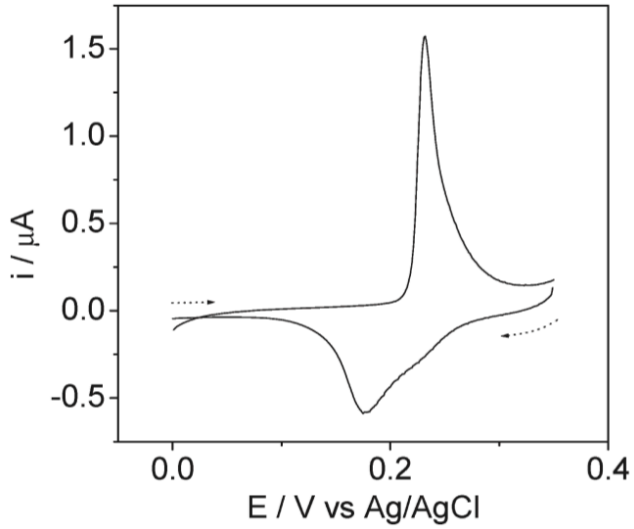

Fig.17– CV recorded in 0.1 M KOH for $Ni(OH)_2$ modified ($\Gamma \sim 20$ nmol cm^{-2}) BDD. Taken from Ref.031.

By calculating the charge associated with oxidation (Q_{ox}) of Ni^{2+} and subsequent reduction (Q_{red}) of Ni^{3+}, a value of $Q_{ox}/Q_{red} \sim 1$ was obtained. This leads to the formation of Eqn.4, for the calculation of the amount of deposited $Ni(OH)_2$ as an effective surface concentration, Γ, on the BDD surface.

$$\Gamma = Q_{ox}/nFA \qquad (4)$$

F is the Faraday constant, *n* is the number of electrons transferred in the redox process (*n* = 1, (Ni^{2+} → Ni^{3+})) and *A* is the geometric surface area of the BDD electrode.

The effect of nanoparticle size on electrocatalytic activity was investigated. L.Hutton *et al.*[31] did this by measuring the current during glucose oxidation in an alkaline solution. Fig.18 shows the CV response for the $Ni(OH)_2$ ($\Gamma \sim 20$ nmol cm^{-2}) modified BDD electrode in the presence of 100 μM glucose in 0.1 M KOH (solid line). Also shown (dashed line) is the CV response without the addition of glucose. The inset shows the CV response of the bare BDD electrode in 1mM glucose solution.

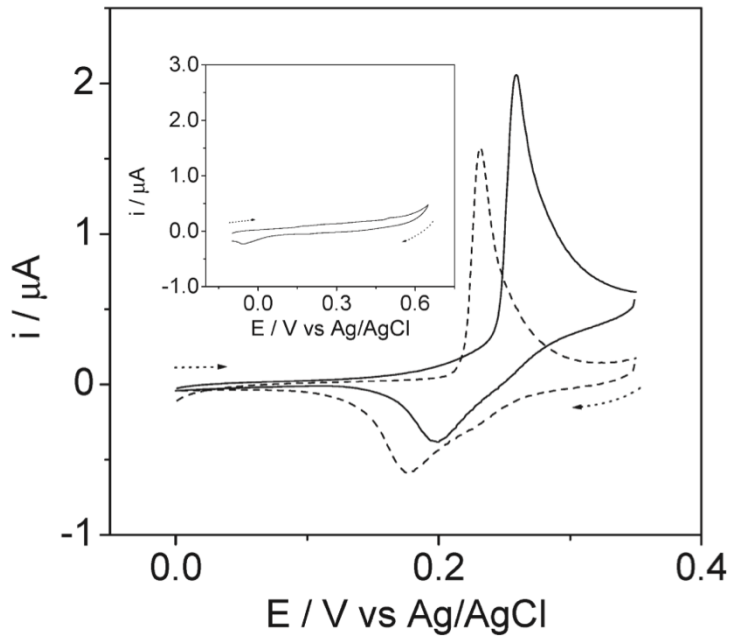

Fig.18 - CVs for the $Ni(OH)_2$ ($\Gamma \sim 20$ nmol cm^{-2}) modified BDD electrode in the presence of 100μM glucose solution, and without. Inset shows bare BDD electrode in the presence of 1mM glucose solution. Taken from Ref.031.

No glucose oxidation was detected for the bare BDD surface. This proves that it is an excellent inert support for $Ni(OH)_2$ nanoparticles in alkaline glucose solutions. Other previously used supports, such as gold, have been shown to interfere with the CV response by contributing to the glucose oxidation.

A clear increase in the anodic current can be seen in the presence of glucose, as well as a decrease in the cathodic current. This is expected for a catalytic process. It was found that the optimal nanoparticle surface concentration for glucose oxidation was $\Gamma \sim 20$ nmol cm^{-2}, which corresponded to nanoparticles ~25 ± 6 nm in diameter with a surface coverage of 85 ± 12 nanoparticles μm^{-2}.

The sensitivity of the electrode (diameter: 1mm) for glucose oxidation was found to be 330 μA mM^{-1} cm^{-2}, with a limit of detection (LOD) of 400nM. This is one of the lowest reported detection limits for glucose using a $Ni(OH)_2$ electrode.

Applications of Microporous Carbon Electrodes

DLC Electrodes for Detection of Hormones

Further research into DLC electrodes was conducted by Silva *et al*.[25] The aim was to use simple, low-cost and fast voltammetry techniques to evaluate the suitability of DLC electrodes for the detection of important hormones, neurotransmitters, and endocrine disruptors. The analytes selected for analysis were dopamine (DA), epinephrine (EP) and acetaminophen (AC).[25]

VACNT forests were prepared, with the CVD DLC film being deposited upon them. Where teepee and honeycombs have been seen before, the length and density of the VACNT forest used here caused a honeycomb structure to form as the VACNT tips stuck together upon film deposition. Fig.19 shows Scanning Electron Microscopy (SEM) images of the sample surfaces.[25]

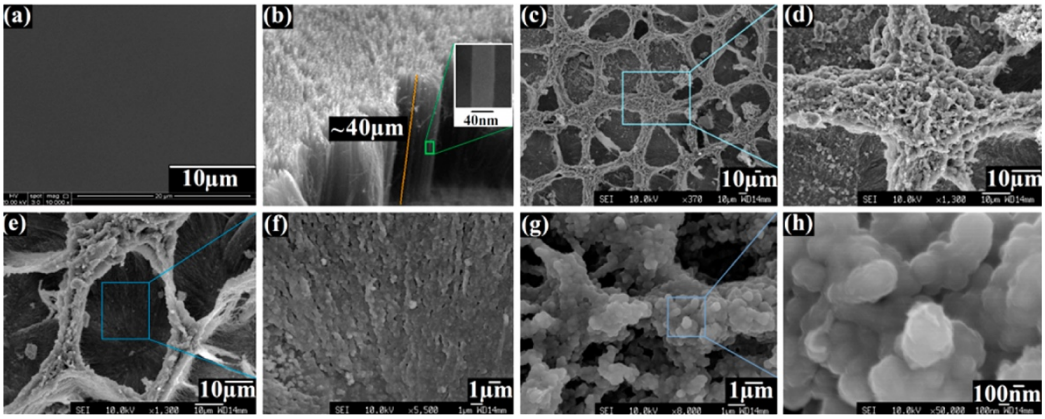

Fig.19 – (a) Flat DLC film, (b) VACNT scaffold used to deposit the DLC film, (c- e) Images of increasing magnification showing the honeycomb structure of the DLC:VACNT structure (f) Higher magnification of the valleys in the honeycomb structure and (g-h) The crests. Taken from Ref.025.

A large range of scan-rates was used in CV experiments to investigate the electron transfer process of the selected molecules on the DLC:VACNT electrodes. 0.2 mol L^{-1} phosphate buffer solution at pH 7.0 was used for all experiments. Table 2 presents the sensitivity results of each analyte.

Table 2 – Sensitivity measurements for detection of DA, EP and AC using the DLC:VACNT electrode. Taken from Ref.025.

Analyte	Sensitivity (µA µmol^{-1} L)	Linear Range (µmol L^{-1})	LOD (µmol L^{-1})
DA	0.27	10-100	3.9
EP	0.29	10-100	4.5
AC	0.28	10-100	2.3

Compared to other electrode materials used for detecting these analytes, the limits of detection are excellent.[25] Repeatability measurements were also performed, with the Relative Standard Deviation (RSD) shown in Table 3.

Table 3 - Repeatability measurements for the DLC:VACNT electrodes showing RSD values. Taken from Ref.025.

Analyte	Concentration (μmol L^{-1})	RSD (%)
DA	30.0	2.9
	50.0	3.5
EP	30.0	1.6
	50.0	1.9
AC	30.0	6.7
	50.0	3.1

The low RSD values (max 6.7%) indicate the high precision of the CV measurements using the DLC:VACNT electrode. These results indicate the promising electrochemical potential of these electrodes, which have a high surface area and are highly sensitive at detecting these analytes at low limits. Further work into detecting other organic and inorganic compounds using DLC:VACNT electrodes are underway.[25]

BDD-Coated bSi Electrodes for Detection of Hormones

Using BDD-coated bSi electrodes to detect dopamine (DA) in an excess of uric acid (UA) is a more clinically relevant test. This was investigated by May *et al.*[30] Experiments for the detection of DA using electrochemical methods have been conducted previously[23]. However, the coexistence of ascorbic acid (AA) and UA cause overlapping voltametric responses when their concentration is much higher than DA, due to their similar oxidation potentials.[30]

Detection of DA, UA and AA simultaneously using traditional flat electrodes is nearly impossible due to their low sensitivity. Metal nanoparticles, CNTs, and polymers are examples of modified materials which have been used to improve electrode sensitivity.

The BDD-coated bSi long-needle electrode was used for the simultaneous detection of DA and UA. Fig.20 shows the differential pulse voltammetry (DPV) curves with both DA and UA present, whilst concentrations of both were being varied. DPV was chosen as a more sensitive voltammetry technique.[30]

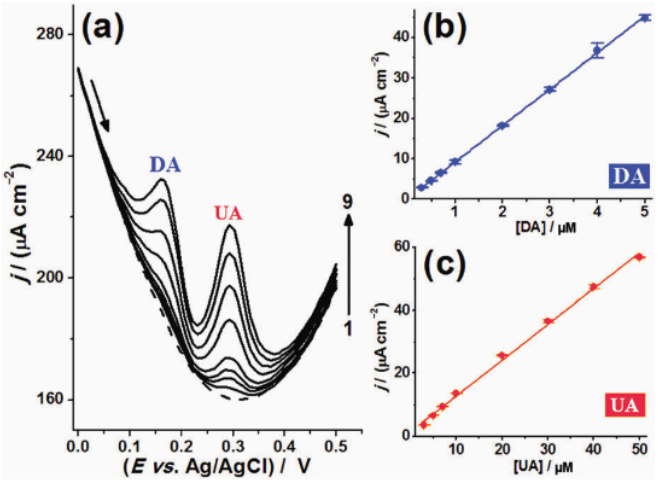

Fig.20 - (a) DPVs recorded in 0.2M phosphate solution containing 9 different DA and UA concentration levels (DA = 0 - 5.0 × 10^{-6} M, UA = 0 - 5.0 × 10^{-5} M) using BDD-coated bSi long- needle electrode. (b) Current density (μA cm^{-2}) vs. concentration of DA (μM), linear best fit. (c) Same as (b), but for UA. Taken from Ref.030.

Table 4 shows the sensitivity measurements calculated from the DPVs for the simultaneous detection of DA and UA using the BDD coated long-needle bSi electrode. High sensitivities and low LODs were achieved using this electrode as an electrochemical sensor.

Table 4 - Range of concentrations over which DA and UA can be simultaneously detected, as well as their analytical sensitivities and LODs. Taken from Ref.030.

	DA	UA
Range/μM	0.30-0.50	3.0-50
Analytical sensitivity/(μA cm^{-2} M^{-1})	9.0	1.1
LOD/μM	0.27	2.1

Repeatability measurements were taken at 9 different increasing concentrations of DA and UA. The RSDs can be seen in Table 5.

Table 5 - RSD values at high and low concentrations of analytes. Taken from Ref.030.

	DA	UA
Low Concentration (RSD, %)	~ 0.65	~ 1.1
High Concentration (RSD, %)	~ 0.51	~ 0.53

This demonstrates the high precision and stability of response from these BDD- coated bSi electrodes as electrochemical sensors.[30]

A Diamond-Based Electrode for Detection of Neurochemicals in the Human Brain

Deep brain stimulation (DBS) is a surgical technique used to treat a variety of neurological disorders including Parkinson's disease, essential tremor, and epilepsy, which are linked to abnormal neurochemical concentrations.[33] DBS involves implanting electrodes within certain areas of the brain. These electrodes produce electrical impulses that regulate abnormal impulses.[34] A pacemaker-like device is implanted in the chest of the patient which controls the amount of stimulation in DBS.[34] Fig.21 shows a diagram of a DBS device.

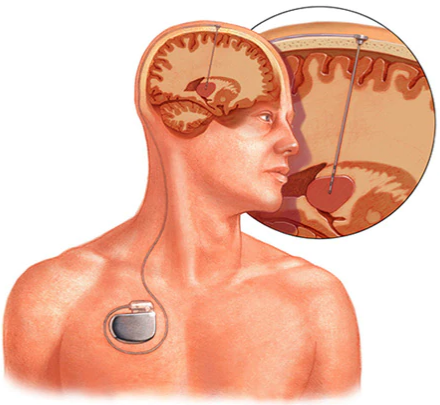

Fig.21 - DBS implant diagram. Taken from Ref.034.

Existing devices rely on open-loop pre-programmed stimulations, i.e. they do not react in real-time to abnormal neurochemical events. Hence, the goal of current research is to produce an implantable closed-loop device that can detect neurochemical concentrations to drive DBS stimulation in real

time, to improve outcomes and reduce adverse effects. Ideally, the device will last throughout the patient's lifetime.[33]

The wireless instantaneous neurochemical concentration sensing (WINCS) system is an example of a closed-loop device. This provided real-time, *in vivo* neurochemical monitoring during DBS surgery using carbon fibre microelectrodes (CFMs). This worked using fast-scan CV (FSCV).[33]

The foundations of a chronically implantable closed-loop DBS device could be formed by integrating WINCS with a neurochemical sensing electrode, along with a feedback control algorithm. However, the current CFM electrodes are not mechanically and electrochemically stable enough to last throughout the patient's lifetime.[33]

BDD electrodes represent an alternative. The aim of Bennet *et al*.[33] was to use BDD electrodes in FSCV, as well as to evaluate the suitability of diamond electrodes in human patients. They tested BDD microelectrodes for real-time neurochemical release *in vivo* (in the patient, to illustrate efficacy) and *in vitro* (outside the patient, to illustrate longevity) in human patients suffering from Parkinson's disease or essential tremor.

The electrodes were prepared by depositing CVD BDD films on sharpened tungsten rods, as shown in Fig.22. Crystals were approximately 0.5 – 2μm in diameter, with a film thickness of approximately 5 - 10μm. The electrode tips were 50μm in diameter, with a length of 100μm, giving a total surface area of around 10,000 μm^2. The electrodes were characterised by Raman spectroscopy, shown in Fig.22f, with the sharp peak at 1332cm^{-1} corresponding to sp^3 hybridised carbon atoms. The broad band at around 1500cm^{-1} correlates to small amounts of sp^2 hybridised carbon atoms, with the weak bands at 1230cm^{-1} and 550cm^{-1} correlating to boron incorporation and accumulation respectivelty.[35]

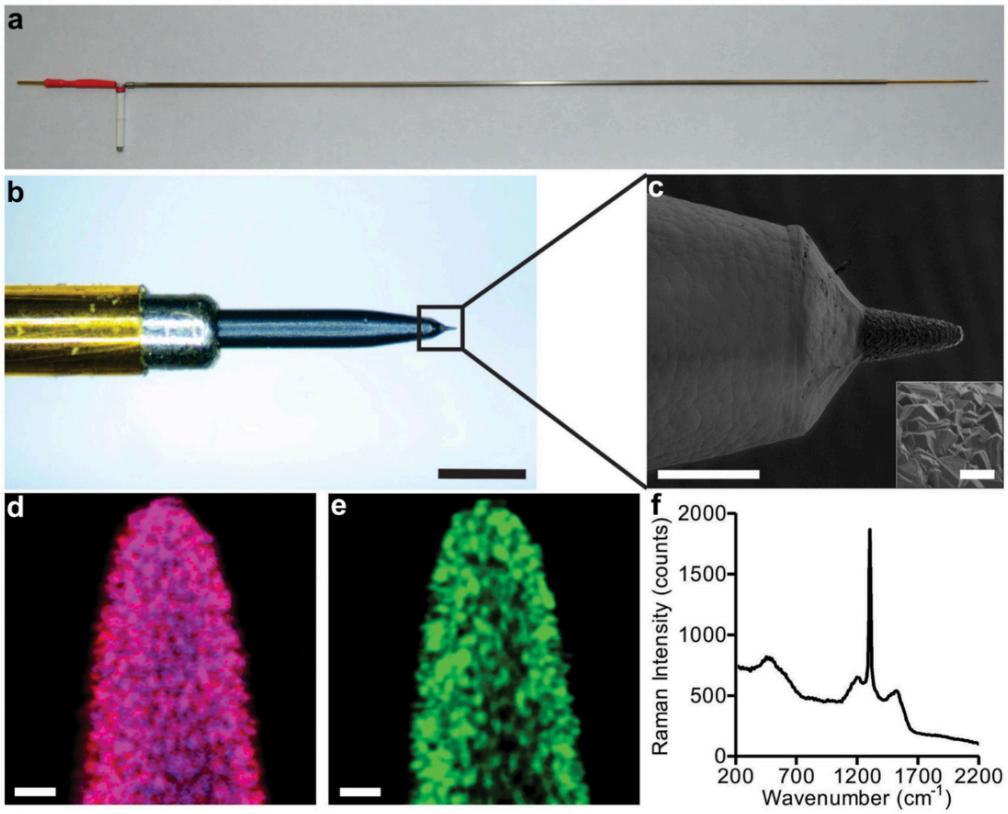

Fig.22 - (a) Full-scale electrode, scale 25nm. (b) Detailed magnification of the electrode tip, scale 500µm. (c) SEM image of electrode tip, scale 100µm. (d,e) Raman spectral map images of electrode tip. Blue depicts BDD, red depicts diamond and green depicts sp^2 carbon. The pink colour in (d) is a combination of red and blue. (f) Raman spectrum of electrode tip. Taken from Ref.033.

Dopamine was selected as the test analyte, as the oxidation and reduction responses using CFMs have been well documented. A CFM and a BDD electrode were subjected to *in vitro* FSCV for a period of time up to 144hrs. Fig.23 shows SEM images of the CFM and BDD electrodes, along with their calibration curves for dopamine detection.[33]

Sensitivity decreased throughout the experiment for both electrodes. The BDD electrode decreased in sensitivity by 16.1% after 144hrs, as shown in Fig.23i. The CFM decreased in sensitivity by 89.4% after 144hrs, shown in Fig.23i. After 144hrs of use, equating to 5.2 million measurement cycles, the CFM had become effectively useless as a dopamine sensor, whereas the BDD electrode retained 83.9% of its initial sensitivity. If the implant was chronic, 5.2 million scans would be roughly equivalent to a scan every 2 mins for 20 years.[33]

Both electrodes were subjected to SEM imaging, shown in Fig.23a-f. The BDD electrode showed no obvious changes, whereas the CFM had been completely eroded. Following strength testing, given the softness of brain tissue and the small diameter of the CFM electrodes, the 0.1 – 0.15g of insertion force can be withstood. However, any asymmetric application forces will lead to the breakage of the electrode tip. The stronger BDD electrode was found to be far more forgiving.[33]

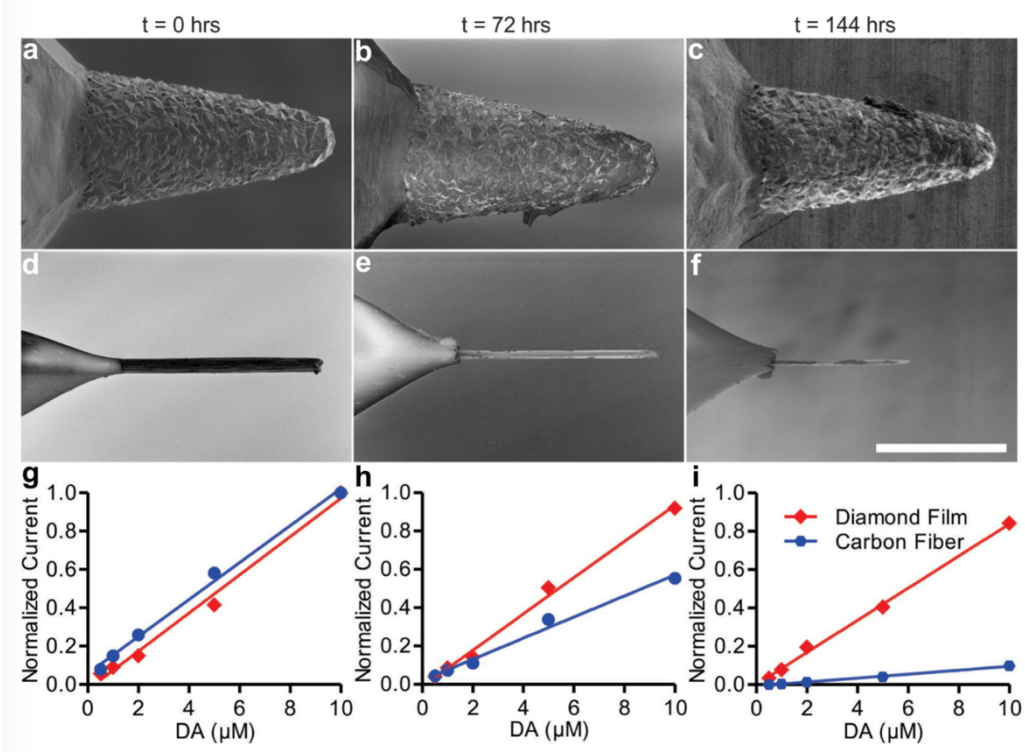

Fig.23 - (a-c) SEM images of the BDD electrode. (d-f) SEM images of the CFM. (g-i) Calibration curves for BDD and CFM electrodes for the detection of dopamine at continuous use. Taken from Ref.033.

DBS lead implantation often leads to tremor reduction without electrical stimulation from the implant.[36] This is referred to as the "microthalamotomy effect". Whilst the exact mechanism is unknown, it is believed that the effect may be mediated by the release of the neurochemical adenosine.[36]

Fig.24 depicts a representative patient suffering from essential tremor. The "microthalamotomy effect" caused a release of adenosine, that was sufficient enough to cause an almost total cessation in the patient's tremor. Figs.24d and 24f show tremor measurements prior to DBS lead placement, with Figs.24e and 24g showing post-placement measurements.[33]

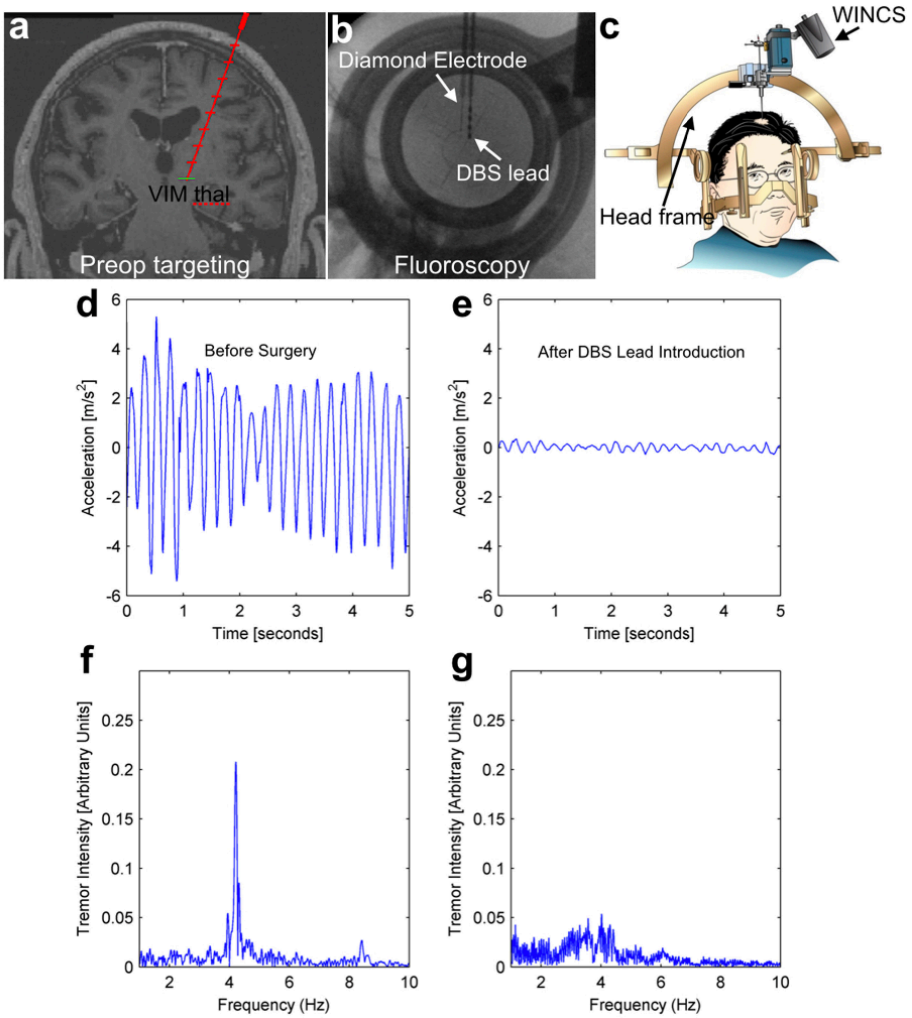

Fig.24 – (a – c) The DBS lead was inserted into the ventral intermediate (VIM) nucleus of the thalamus of an essential tremor patient. A wireless accelerometer was worn to measure tremor. Prior to surgery, a pronounced tremor at 4.2Hz was measured (d, f), however after lead placement, a cessation of the tremor was caused by the microthalamotomy effect with no applied voltage (e, g). Taken from Ref.033.

To demonstrate the *in vivo* suitability of the BDD electrodes for their intended purpose in humans, proving that the electrodes could detect changes in adenosine concentration was vital. A volunteer test patient undergoing DBS lead placement for Parkinson's disease was recruited. The BDD electrode was inserted into the target region first before the insertion of the DBS electrode. Mechanical release of adenosine due to the microthalamotomy effect was observed through the BDD electrode. Signature peaks at +1.0V and +1.5V are indicative of adenosine oxidation.[33]

The sensitivity of the CFM and BDD electrodes in humans were compared and are presented in Fig.25. The biochemical makeup of the human brain is more complex than the pure adenosine in the flow cell. However, the signature peak at +1.5V can be seen which correlates to adenosine oxidation. This peak was present in all cases.[33]

It is clear in Fig.25b and 25d that the BDD electrode is less sensitive to the second oxidation peak at +1.0V. However, it does demonstrate that detection of adenosine by the BDD electrode is possible, showing promise to fulfil the desired outcome of producing a closed-loop DBS device.[33]

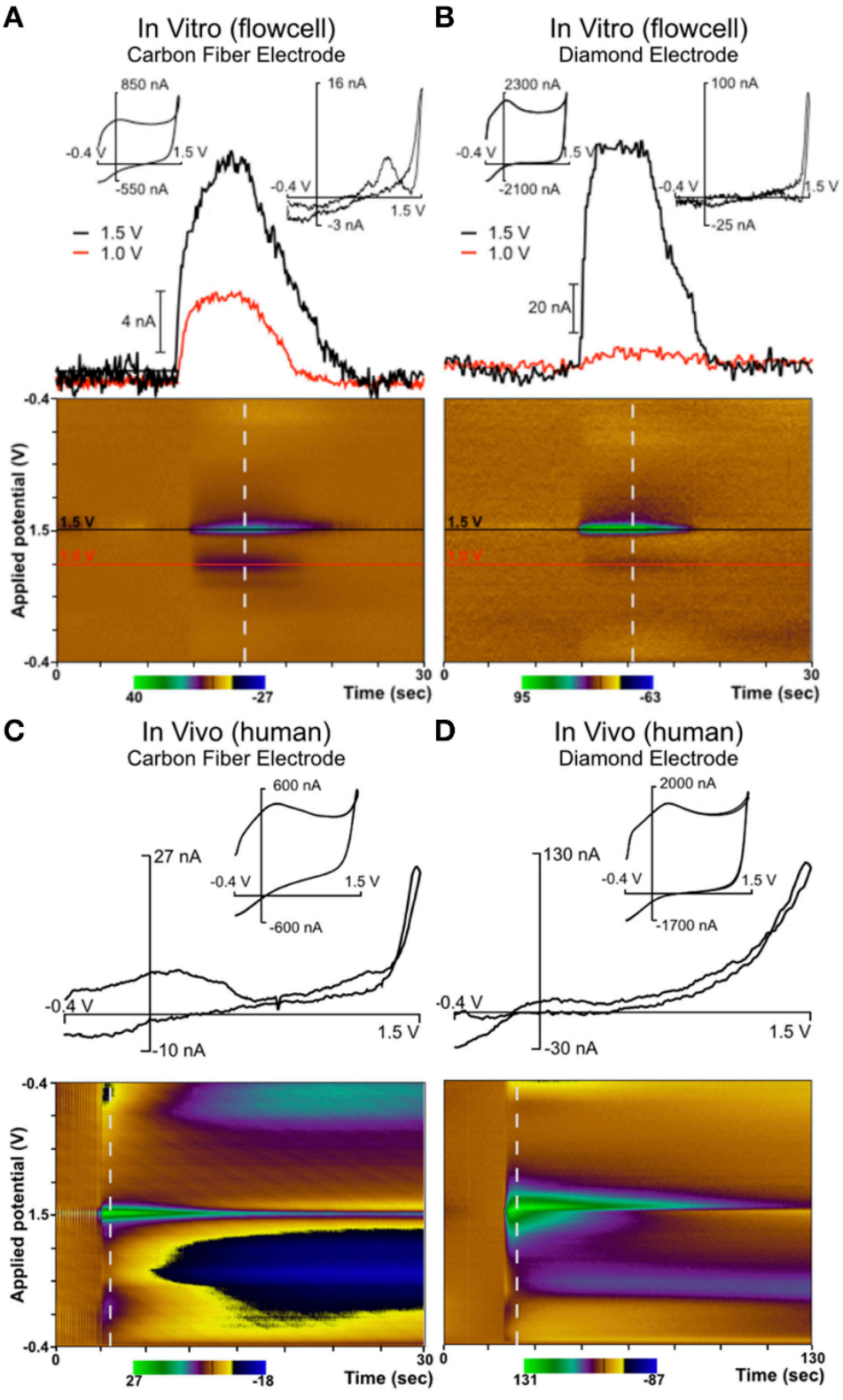

Fig.25 – Comparison of BDD electrode with a CFM electrode in a flow cell and in vivo. *The microthalamotomy effect can be seen in both cases, producing an adenosine-like signal. (a) CFM electrode* in vitro, *(b) BDD electrode* in vitro, *(c) CFM electrode* in vivo, *(d) BDD electrode* in vivo. *Taken from Ref.033.*

Electrochemical Oxidation of Pharmaceuticals using a BDD Electrode

Preventing wastewater from polluting our environment is one of the main topics in water research.[37] Pharmaceutical pollutants have received particular attention, originating mainly from hospitals and care homes. Pollutants enter the environment through sewage and wastewater treatment plants, causing a wide variety of unwanted effects on organisms living in surface and ground water. Pollutants have also been detected in drinking water.

Electrochemical oxidation (EO) is a viable method for the removal of these substances from wastewater. This is an attractive technique, as it does not require additional chemicals and operates at ambient temperature. Previously, the use of EO in wastewater treatment has been reported, but effective degradation was not achieved until diamond coated anodes were used.[37]

Diamond coated anodes have a high overpotential for water hydrolysis. This generates hydroxyl radicals at the anode's surface with high efficiency. The hydroxyl radicals go onto serve as the oxidants for the degradation of organic pollutants. A simple diagram showing an example diamond wastewater treatment system is shown in Fig.26.

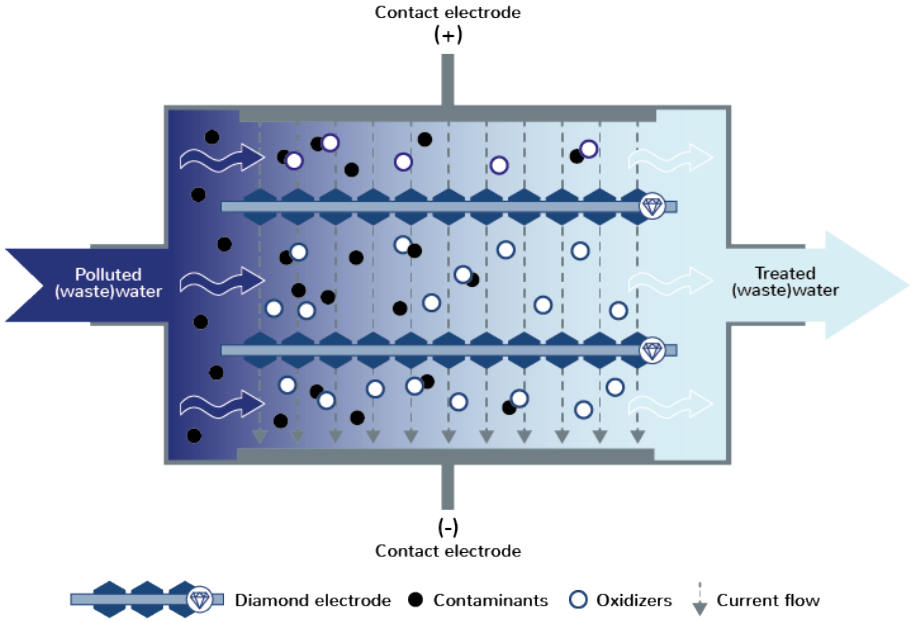

Fig.26 - Example diamond wastewater treatment system. Taken from Ref.038.

Loos *et al.*[37] aimed to evaluate the degradation of four pharmaceuticals using BDD electrodes. These are shown in Table 6.

Table 6 - Pharmaceuticals chosen for analysis. Taken from Ref.037.

Pharmaceutical	Use
Iopromide (IOP)	X-ray contrast agent.
Sulfamethoxazole (SMX)	Antibacterial agent.
17-alpha-ethinylestradiol (EE2)	Steroid derivative used in contraceptives.
Diclofenac (DCF)	Non-steroidal anti-inflammatory drug.

The influence of flow rate (Q) , temperature (T) and current (I) were evaluated. Prior to testing, a simulated effluent wastewater (SWW) solution was prepared by dissolving the four pharmaceuticals. The results were then compared to real effluent wastewater (RWW), which was collected from a hospital treatment plant.[37]

The experimental setup consisted of a flow through electrochemical cell (similar to Fig.26), a circulation tank and a centrifugal pump. The tank was filled with 10L of the experimental solution before each experiment, prior to being circulated at a fixed flow rate through the cell. A conductive Si substrate, coated with a BDD layer (surface area 189cm^2), was used as the electrode.[37]

Initially, the kinetics for degradation of each pharmaceutical in SWW were assessed on their own and then in a mixture. Fig.27 shows the pharmaceutical concentration vs time of treatment for the SWW with each compound individually, and then in a mixture.[37]

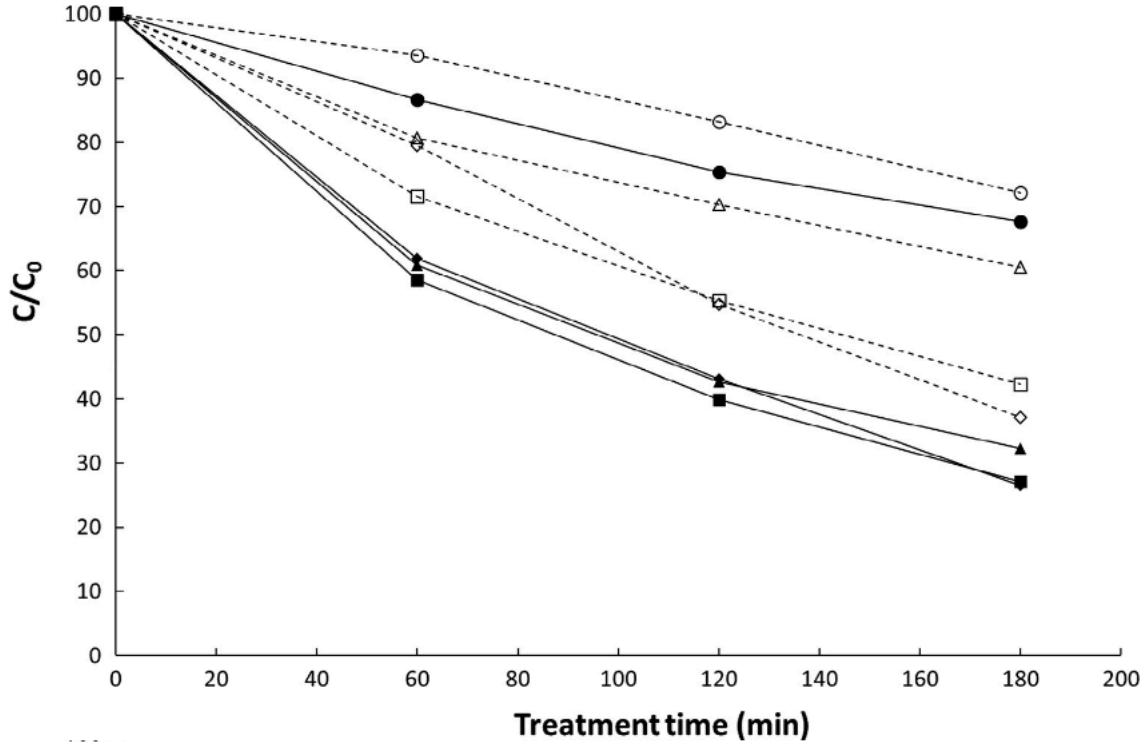

Fig.27 - Symbols indicate IOP (●/O), SMX (■/□), EE2 (▲/△) and DCF (♦/◊). Compound concentration vs time during BDD treatment for the SWW with each compound individually (closed symbols, full lines) and a mixture of all compounds (open symbols, dashed lines). Taken from Ref.037.

When the pharmaceuticals were added to the SWW individually, only small changes were observed between the degradation curves of SMX, EE2 and DCF, with degradations of 72.9%, 69.7% and 73.7% respectively. IOP degradation was much slower, with only 32.3% degraded after 180 mins.[37]

When mixed, the degradation rate was considerably lower for all compounds, with degradations of 27.8%, 67.7%, 39.5% and 66.9% for IOP, SMX, EE2 and DCF respectively. The decrease in degradation for EE2 was particularly large. First order reaction rate constants (k) were determined and are shown in Table 7. The correlation coefficients (R^2) show the concentration measurements were highly accurate. The order of reaction rate constants is the same for both individual and mixed samples, with DCF ≅ SMX > EE2 > IOP.[37]

Table 7 - Rate constants for the degradation of IOP, SMX, EE2 and DCF in SWW for each compound individually and in a mixture. Taken from Ref.037.

Compound	k (min^{-1})	R^2
IOP (individual)	0.0023	0.996
IOP (mixed)	0.0019	0.972
SMX (individual)	0.0074	0.990
SMX (mixed)	0.0050	0.996
EE2 (individual)	0.0064	0.980
EE2 (mixed)	0.0029	0.989
DCF (individual)	0.0075	0.997
DCF (mixed)	0.0058	0.989

Competitive degradation between the pharmaceuticals leads to the decrease in rate constants. The amount of hydroxyl radicals generated on the surface of the BDD electrodes is constant, given the set of process conditions (I = 0.9A, Q = 250 L/h and T = room temperature). When all compounds are added simultaneously, a competitive use of the hydroxyl radicals for degradation occurs. Without addition of any pharmaceutical compounds, the SWW contains 60 mg/L of organic material. Adding 0.5 mg/L of each pharmaceutical increases this concentration to 62 mg/L. This is small compared to the overall concentration of organic compounds. Therefore, the large decrease in k between the individual and mixed readings, when only a small amount of organic matter has been added to the SWW, suggests that the pharmaceuticals are targeted specifically by the EO treatment.[37]

Flow rate (Q) influence on the electrochemical cell was investigated by measuring pharmaceutical degradation over time at three different flow rates (Q = 125, 250 and 500 L/h). It was found that flow rate has a limited effect on the degradation kinetics, meaning the occurring degradation reactions are reaction rate limited, as opposed to mass transfer limited.[37]

The effect of temperature (T) was evaluated next. Temperatures of 18, 30 and 50°C were used, with 0.5mg/L of each pharmaceutical being added simultaneously to the SWW (I = 0.9A, Q = 500 L/h). The results are shown in Fig.28, with the rate constants shown in Table 8.

Table 8 - Degradation rate constants for IOP, SMX, EE2 and DCF in SWW at different temperatures. Taken from Ref.037.

T (°C)	IOP		SMX		EE2		DCF	
	k (min^{-1})	R^2	k (min^{-1})	R^2	k (min^{-1})	R^2	k (min^{-1})	R^2
18	0.0016	0.995	0.0021	0.973	0.0039	0.964	0.0062	0.976
30	0.0018	0.986	0.0040	0.976	0.0049	0.977	0.0064	0.998
50	0.0023	0.989	0.0060	0.976	0.0062	0.991	0.0102	0.972

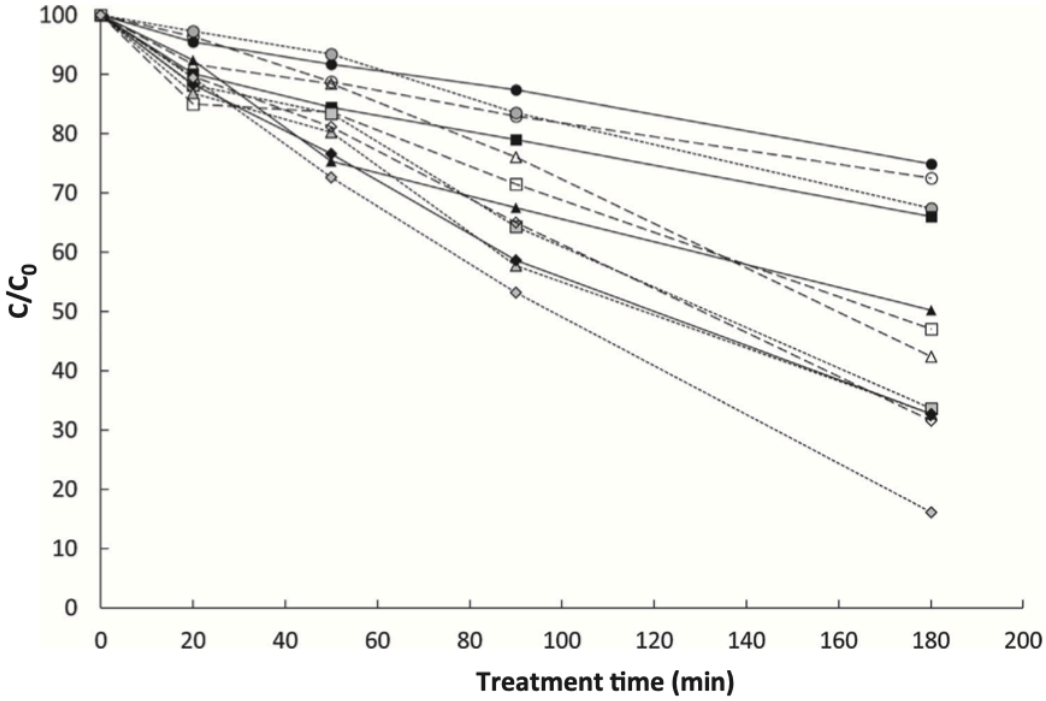

Fig.28 - Compound degradation vs time at different temperatures. IOP (●), SMX (■), EE2 (▲) and DCF (♦). The appearance of the lines indicates the temperature, with 18 °C (full symbols and full lines), 30 °C (open symbols and dashed lines), 50 °C (grey symbols and dotted lines). Taken from Ref.037.

The degradation rate constants for all pharmaceuticals increased with temperature. *k* increased by 44%, 186%, 58% and 64% for IOP, SMX, EE2 and DCF respectively, between 18-50°C. The 186% increase in *k* for SMX is particularly high, with the other three components showing a less pronounced increase in *k*.[37]

Finally, degradation experiments were performed on RWW, and the effect of current was also assessed. All four pharmaceuticals were added to the RWW simultaneously, at two separate concentrations of 0.5 mg/L and 10 mg/L each. The treatment time was increased to 540 mins for the 10 mg/L concentration, to allow sufficient degradation of the compounds. The current was set to 0.9 and 3.1A, at a temperature of 50°C. Fig.29 shows the results of the degradation experiments and Table 9 shows the rate constants.

Table 9 - Degradation rate constants for IOP, SMX, EE2 and DCF in RWW. Taken from Ref.037.

	0.5mg/L, 0.9A		0.5mg/L, 3.1A		10mg/L, 3.1A	
	k (min^{-1})	R^2	k (min^{-1})	R^2	k (min^{-1})	R^2
IOP	0.0025	0.962	0.0088	0.973	0.0087	0.976
SMX	0.0252	0.990	-	-	-	-
EE2	0.0177	0.908	-	-	0.0095	0.899
DCF	0.0117	0.992	0.0241	0.894	0.0248	0.962

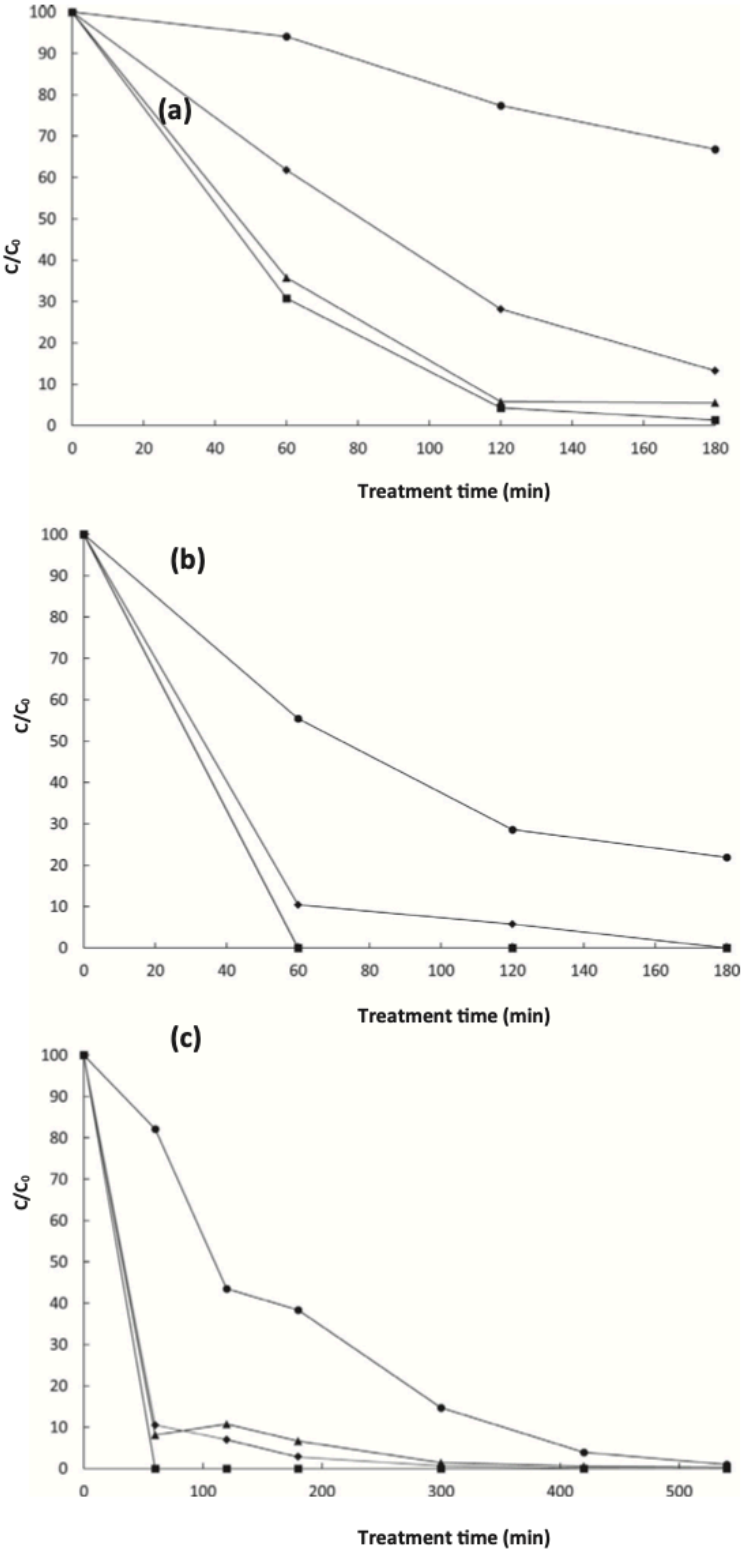

Fig.29 - Compound degradation vs time in RWW. (a) C_0 = 0.5mg/L, Q = 500L/h, I= 0.9A; (b) C_0 = 0.5mg/L, Q = 500L/h, I = 3.1A; (c) C_0 = 10mg/L, Q = 500L/h, I = 3.1A for IOP (●), SMX (■), EE2 (▲) and DCF (♦). Taken from Ref.037.

To assess the difference in degradation efficiency between SWW and RWW, the degradation rate constants for the pharmaceutical compounds at the following conditions were compared: C_0 =

0.5mg/L, I = 0.9A, T = 50°C and Q = 500L/h. The results under these conditions are shown in the final row of Table 8.

For all compounds, there was an increase in *k*, although the relative increase for each largely differed. *k* increased by 19%, 367%, 378% and 72% for IOP, SMX, EE2 and DCF respectively.[37]

Chemical oxygen demand (COD) is the measure of the amount of oxygen needed to oxidise the organic matter present in a quantity of water.[39] The COD of the SWW was 53.2mg/L and the RWW was 78.4mg/L.[37]

The increase in *k* for all compounds in the RWW is impressive, as the COD value is ~50% higher than in the SWW. This links to the previous discussion on the selectivity of oxidation. It appears that the type of organic matter in the RWW consumes less oxidative species and has higher selectivity towards the added pharmaceuticals.[37]

Faster degradation of all compounds was observed when the current was increased to 3.1A. After the first sampling point at 60 mins, the concentration of SMX and EE2 had decreased below the detection limit, hence why there are blank values in Table 8. For IOP and DCF, *k* increased by 252% and 106% respectively. Increasing C_0 to 10 mg/L whilst maintaining the current had a marginal effect on *k*.[37]

Degradation Products

It occurred to Loos *et al*.[37] that the degradation products of the pharmaceutical compounds may be difficult to remove from wastewater. Fig.30 shows a chromatogram obtained for DCF after 0, 60, 120, 180 and 300 mins of EO treatment using a BDD electrode, with the same experimental conditions as Fig.29.

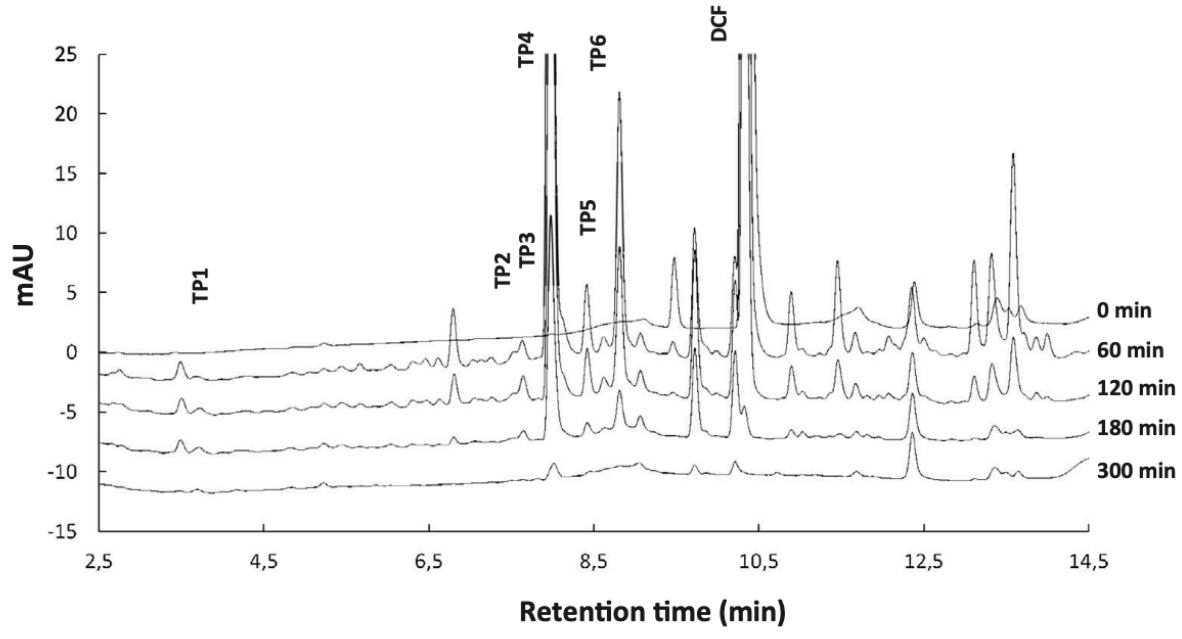

Fig.30 – Chromatogram of DCF and its main degradation products after 0, 60, 120, 180 and 300 mins of treatment. Taken from Ref.037.

There are clearly a number of degradation products seen in the wastewater after the DCF has been completely degraded. Loos *et al.*[37] were unable to accurately determine the structures of the degradation products. Fig.31 shows the concentration of degradation products over time. DCF can be

seen to be completely removed from the wastewater after 180 mins. However, it takes two to three times longer to remove the degradation products from the solution. These results were similar for SMX, EE2 and IOP.

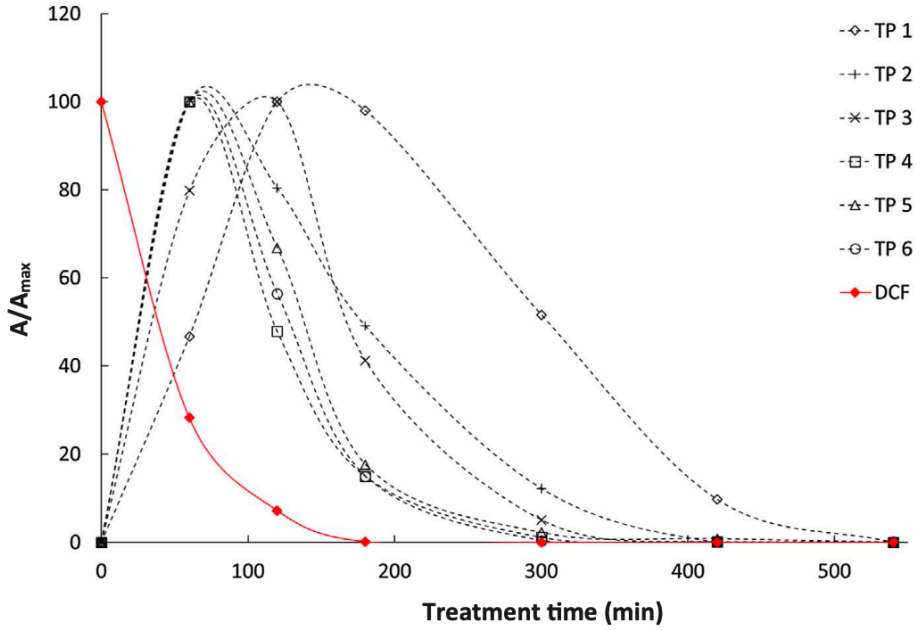

Fig.31 – Change in concentration of DCF and its degradation products as a function of time. The area under the curve (A) is plotted as a function of the maximum observed area under the curve (A_{max}) for each compound. Taken from Ref.037.

Monitoring the removal efficiency of the parent compound is therefore not sufficient, as the degradation products may have higher longevity in solution, as well as potentially higher toxicity.[37]

BDD electrodes were shown to be an effective method for removing pharmaceutical compounds from RWW. Variations in temperature, current and flow rate allowed for optimisation of the BDD electrode system. However, it should be considered that the removal of degradation products from the parent compound can take 2-3 times longer.[37]

Experimental

Fabrication of Flat Diamond Samples

Flat BDD samples were synthesised using hot filament CVD (HFCVD). Initially, 10x10mm samples of 'special' Si were prepared. 'Special' Si refers to the highly doped Si structure which makes it conductive. A laser cutter was used to mark the dimensions of the samples on the Si surface, before being cut to the right size manually. Nanodiamond seed crystals were then placed on top of the Si, before being massaged over the entire surface. This created a rough and dull surface, as shown in Fig.32.

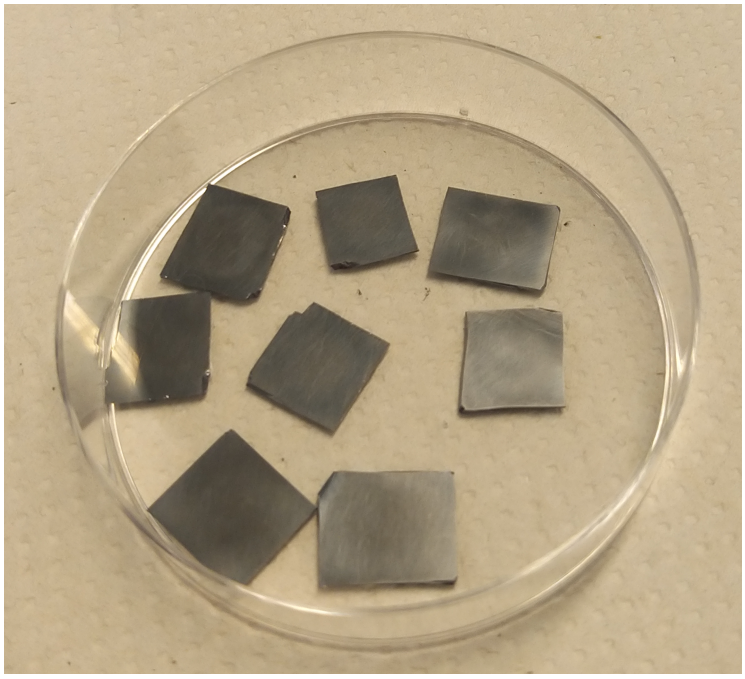

Fig.32 - Flat diamond samples after seeding before deposition.

The samples were then placed in the HFCVD reactor. The gaseous mixture comprised of B_2H_6 (1000 standard cubing centimetre per minute (sccm)), H_2 (200 sccm) and CH_4 (20 sccm), with a reactor pressure of 20 torr. A growth time of 6hrs was used. The current was set to 25A and was adjusted regularly to keep it constant throughout the growth time. The final 2mins of growth were in H_2 only, to ensure the diamond was H-terminated.

Fabrication of Black Diamond Samples

10x10mm bSi samples were prepared, using manual cutting techniques, to ensure no damage to the surface from a laser cutter. A diamond seed solution was then prepared. The nanodiamond seed crystals used for the flat diamond samples could not be used on bSi, as spreading them to ensure total surface coverage would have damaged the delicate needles.

10 drops of nanodiamond colloid solution were deposited into a methanol-cleaned sample tube. The sonication machine was wiped clean with methanol. The nanodiamond colloid was diluted with methanol until the sample tube was 90% full. This was clamped to the sonicating machine, so the needle was nearly at the bottom of the sample tube. The solution was sonicated for 3hrs. After this

time, the methanol level had decreased. This was replenished to 90% full and sonicated for a further 15mins.

Roughly 30% of the nanodiamond solution was poured into a petri dish and the bSi samples were submerged for 1hr of deposition. The samples were then transferred to a hot plate and heated at 50°C for 20mins to evaporate the excess methanol. This process was repeated twice more, such that the total deposition time was 3hrs and the total drying time was 1hr.

Fig.33 shows one of the prepared samples. The surface should be one uniform colour, although clear markings can be seen on the surface which was consistent with every sample prepared. Initially, this was thought to be drying marks left from impurities in the methanol, however SEM imaging was needed to confirm this.

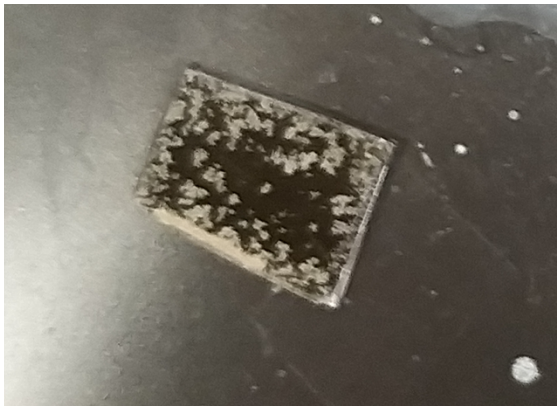

Fig.33 - One of the bDi samples showing clear markings after deposition and heating.

The bDi samples were then placed in the HFCVD reactor under the same conditions as used for the flat Di samples, with a shorter growth time of 40mins. These were also H-terminated.

Electrochemistry of Diamond Samples

One flat Di and one bDi sample were taken to the electrochemistry lab for analysis. An electrode was prepared with the assistance of A.Black. To prepare the flat Di electrode, a wire connection was made to the back of the sample via the special Si substrate.

The bSi substrate used for the bDi electrode is insulating, as opposed to the highly conducting special Si substrate used for the flat Di sample. This means that the wire connection must be made on the bDi side of the sample, rather than the back of the substrate. Teflon tape with a circular hole of 3mm diameter was applied to the bDi side of the sample. This was pressed down with tweezers to ensure it was sufficiently stuck to the surface, with a section at the top left unstuck to allow attachment of a wire. Silver paint was then applied to the wire and the sample, before being allowed to dry overnight to create a connection.

Next, the tape above the wire was reapplied on top of the silver paint connection. Again, tweezers were used to ensure the tape was completely stuck to the surface. Teflon tape was wrapped around all parts of the electrode, except the exposed 3mm hole. This should guarantee that no other parts of the electrode are exposed to the electrolyte, giving confidence that the electrode surface area is known. This gives an exposed geometrical surface area of ~ 7mm^2, which was used as the effective surface area in future calculations.

The disadvantage of using this method to prepare the electrodes is that it relies on there being full conductivity across the film between the exposed area and the wire contact.

100cm^3 of 1mM ruthenium hexamine ([Ru(NH$_3$)$_6$]Cl$_3$) and 100mM KCl in deionised water was prepared as the electrolyte solution. Graphite was used as the counter electrode and Ag/AgCl (3M KCl) as the reference electrode. The electrolyte was degassed by bubbling argon through the solution. This removes any dissolved oxygen to ensure oxygen reduction does not interfere with the experiment. The bDi electrode was soaked in the electrolyte solution for 2hrs to allow the solution to penetrate down to the depths of the needles.

Cyclic voltammograms were then produced, at scan rate 0.05V/s and a potential range of -0.30V to 0.05V. Fig.34 shows the resultant CVs.

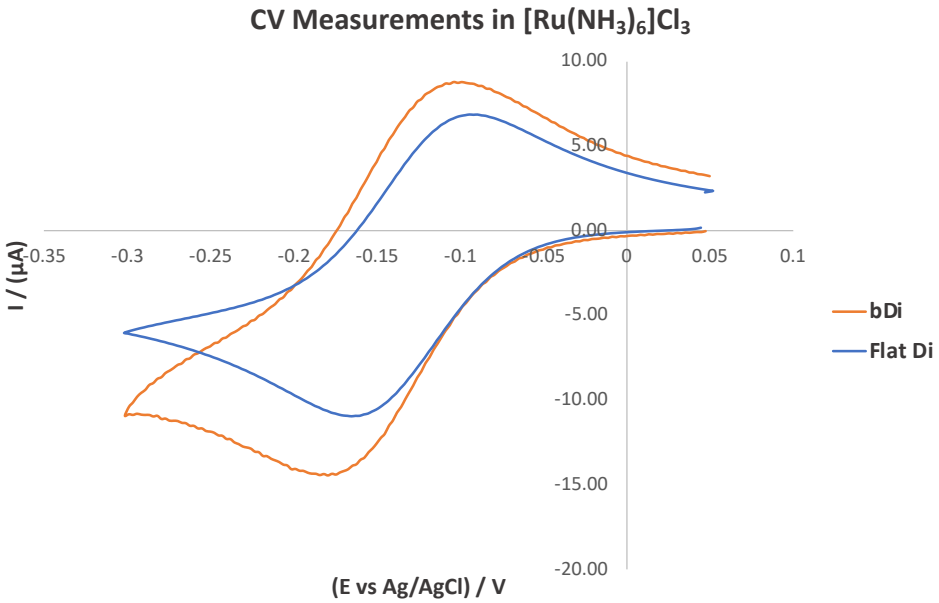

Fig.34 - CVs from bDi and flat Di electrodes at scan rate 50mV/s within a potential range of -0.30 to 0.05V. 1mM [Ru(NH$_3$)$_6$]Cl$_3$ in 100mM KCl electrolyte solution.

The results were unexpected, as the CVs for flat Di and bDi look similar. The surface area of the bDi electrode was expected to be much higher than the flat Di, however the similar area inside the two CVs shows this is not the case.

Positively, the connection made between the bDi electrode and the wire via the silver paint seems to be successful. A poor connection would lead to an increase in resistance and the peak separation between the flat Di and the bDi CVs would be noticeable, however, this is not the case.

SEM Analysis

SEM imaging was then used to determine the reason for the lower-than-expected surface area of the bDi. Figs.35 and 36 show top-down SEM images of the flat Di and the bDi samples respectively at 10,000x magnification.

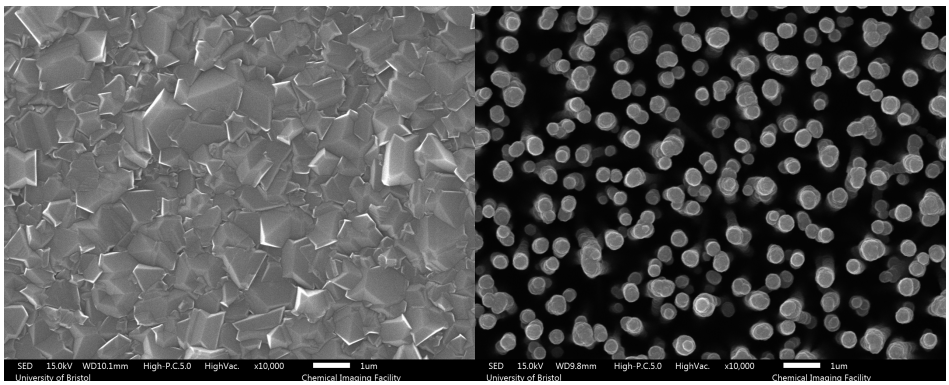

Figs.35 and 36 – SEM images at 10,000X magnification of (Left) Top-down view of flat Di sample and (Right) Top-down view of bDi sample.

Upon further inspection, the marks left on the bDi sample surface appeared to be solid build-up. This is shown in Fig.37.

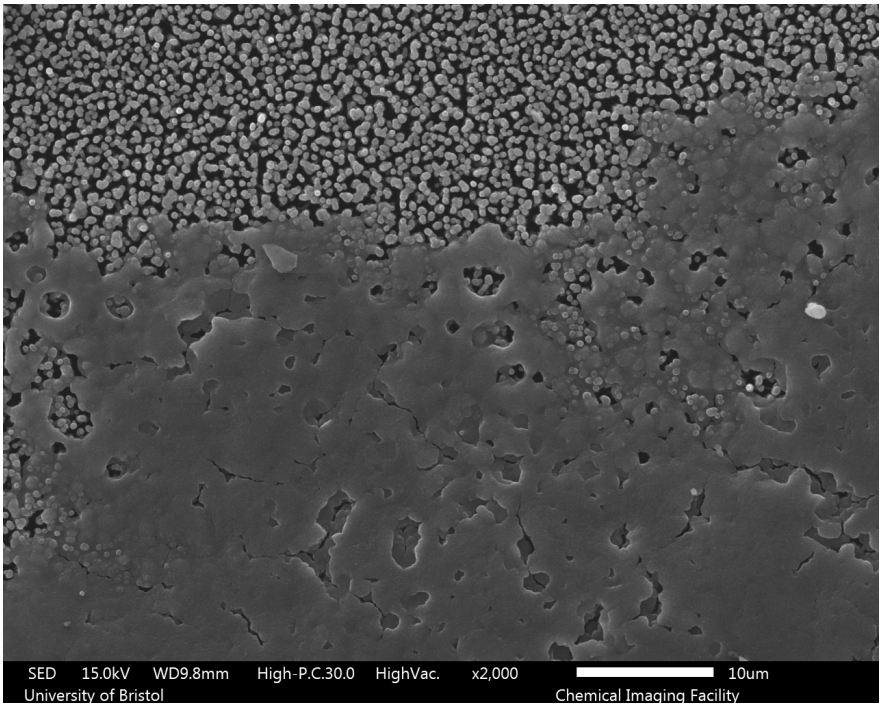

Fig.37 - Solid build-up on the surface of the bDi.

The cause of this build-up is unknown, although it is thought that during the drying of the sample following seeding, the methanol evaporated and brought the nanodiamond seed crystals to the surface with it, which subsequently caused growth of the CVD film on top of the bSi needles, rather than in between them. Nonetheless, the number of these marks on the sample, as seen in Fig.33, clearly indicates that the surface area of the electrode is greatly reduced and resembles more of a flat surface.

Changes to Sample Synthesis

Following SEM imaging, the synthesis method was revisited to determine a cause for the solid deposition. Initially, removing the solid manually was attempted. Three techniques were used, further heating at 50°C, further heating with methanol, and further heating with methanol and a nitrogen gun.

The methanol was sprayed onto the samples whilst being heated. The nitrogen gun was used immediately after spraying the sample with methanol. None of the three techniques were successful.

The seeding process was repeated. On this occasion, two different methods were used on 3 bSi samples each. The nanodiamond colloid solution was prepared using the same method as described previously. The first set of samples (MM15) were immersed in the seeding solution for 1hr, before being heated at 30°C for 30mins. This process was repeated twice more, for a total seeding time of 3hrs and a total heating time of 1.5hrs.

The second set of samples (MM17) were immersed in the seeding solution for 1.5hrs, before being left to dry in air for 1hr. This process was repeated once more, for a total seeding time of 3hrs and a total drying time of 2hrs.On both sets of samples, no markings were present. This is shown in Figs.38 and 39.

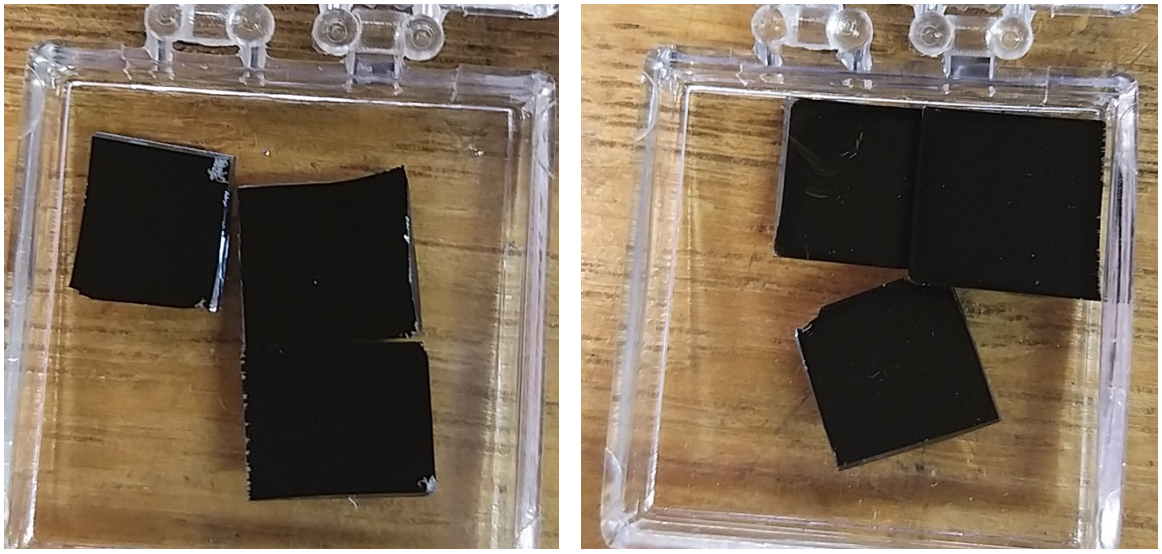

Figs.38 and 39 - bDi samples prepared after (Left, MM15) 3hrs seeding, 1.5hrs heating at 30℃ and (Right, MM17) 3hrs seeding and 2hrs drying in air.

The samples were then placed in the CVD reactor and grown for 30mins under the same conditions as mentioned previously. No new flat diamond samples were made.

SEM Analysis

SEM analysis was undertaken on the new samples. Figs.40 and 41 show the top-down and side-view images of MM15. The top-down view shows that there is no solid build up on the surface. The side-view image shows that deposition has been successful, with diamond crystals visible down the length of the needles and along the bottom surface of the bSi substrate.

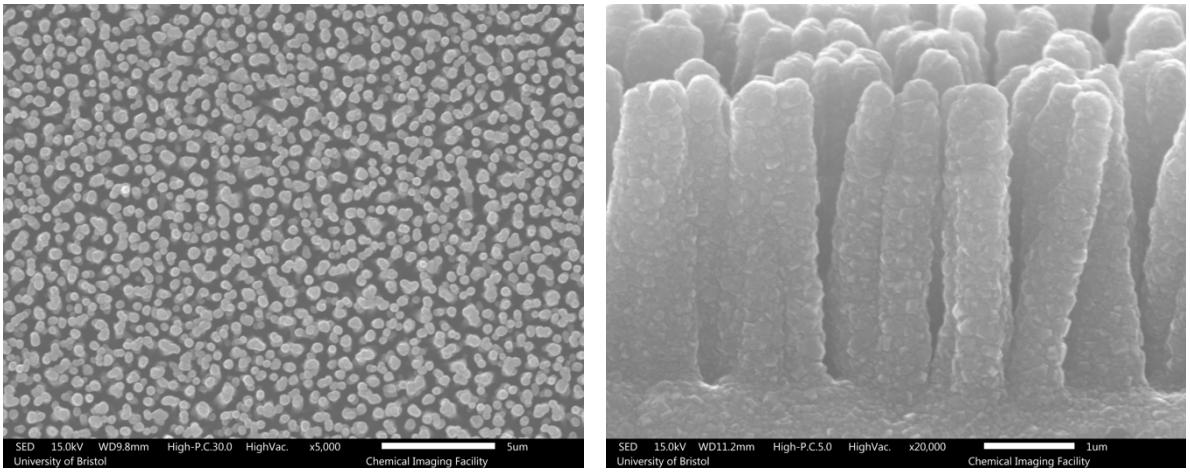

Figs.40 and 41 - Top-down and side-view images of MM15 (3hrs seeding, 1.5hrs heating at 30C).

Figs.42 and 43 show the top-down and side-view SEM images of MM17. Again, there is diamond growth down the length of the needles and along the bottom of the substrate, with no solid build up on the surface.

There are some noticeable differences between the two samples. MM15 has shorter, rounder needles, whereas MM17 has sharper, longer needles. This suggests that the deposition method for MM15 was better, as MM17 resembles the shape of bSi with no diamond growth.

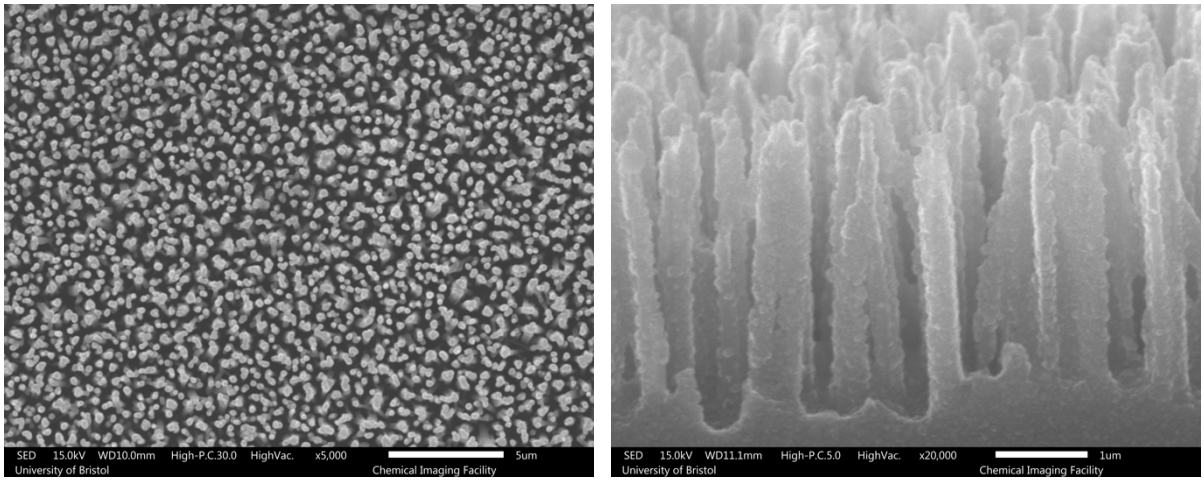

Figs.42 and 43 – Top-down and side-view images of MM17 (3hrs seeding, 2hrs drying in air).

Results

H-Terminated bDi Capacitance

MM15 and MM17 were taken to the electrochemistry lab for analysis. They were analysed using the same processes as May *et al.*[30] Initially, capacitance measurements were taken. 100cm^3 of 100mM KNO_3 was prepared as the electrolyte solution, which was poured into a glass, three-electrode cell. Graphite was used as the counter electrode and Ag/AgCl (3M KCl) as the reference electrode. A scan rate of 50mV/s was used, within a potential range of -0.1V to 0.1V. Fig.44 shows the capacitance plot.

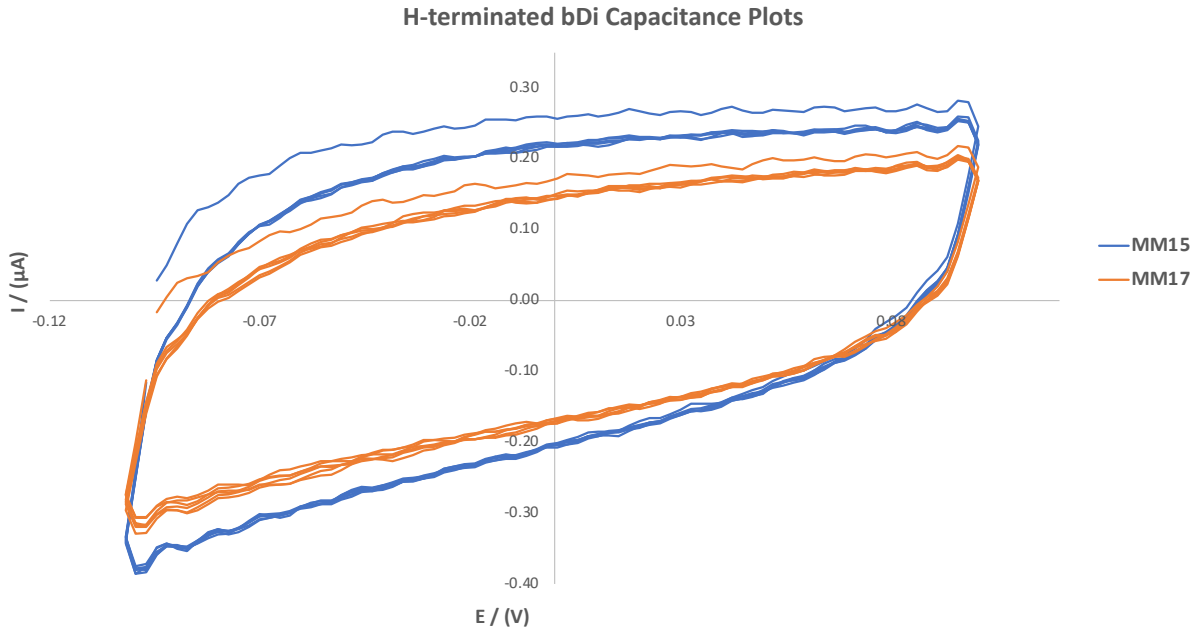

Fig.44 – H-terminated capacitance CVs (v = 50mV/s) in 100mM KNO_3.

The CVs are quasi-rectangular in shape, which shows interfacial double-layer charging has occured.[30] Double layer capacitance values (C_{dl}) were then calculated using[40]:

(5)

$$C_{dl} = i_{av}/vA$$

Where i_{av} is the average current from the forwards and backwards scans at 0V, v is the scan rate and A is the electrode area. Capacitance values for MM15 and MM17 were then calculated, with the results shown in Table 10.

Table 10 - Capacitance values for H-terminated MM15 and MM17.

Electrode	Capacitance / (µF cm^{-2})
MM15	59.7
MM17	44.8

Compared to the data collected by May *et al.*[30] (Table 1) these capacitance values are larger than the BDD-coated bSi short needles, but significantly lower than the long and partially overgrown needles.

To improve these measurements, it was decided that O-termination of the BDD film may have an effect. H-terminated diamond is moderately hydrophobic, due to the lack of oxygen-containing groups on the surface.[41] This may lead to the electrolyte solution being unable to penetrate down to the depths of the needles, due to hydrophilic repulsion, causing an effective decrease in the electroactive surface area of the electrode.

Therefore, O-termination was achieved by treatment with ozone for 30mins before any further electrochemical analysis was undertaken, in the hope that the surfaces would now be hydrophilic. The whole electrodes were placed into the ozone oven (rather than only the bDi samples), so the electrodes did not have to be remade after treatment. A flat, O-terminated sample (MM2) synthesised previously was used as comparison. The capacitance measurements were repeated, under the same conditions as before.

O-Terminated bDi Capacitance

Fig.45 shows the O-terminated bDi capacitance CVs in KNO_3 at a scan rate of 50mV/s. Fig.45a can be found in Section 1 of the appendix, showing the capacitance plots of MM2 and MM17 only.

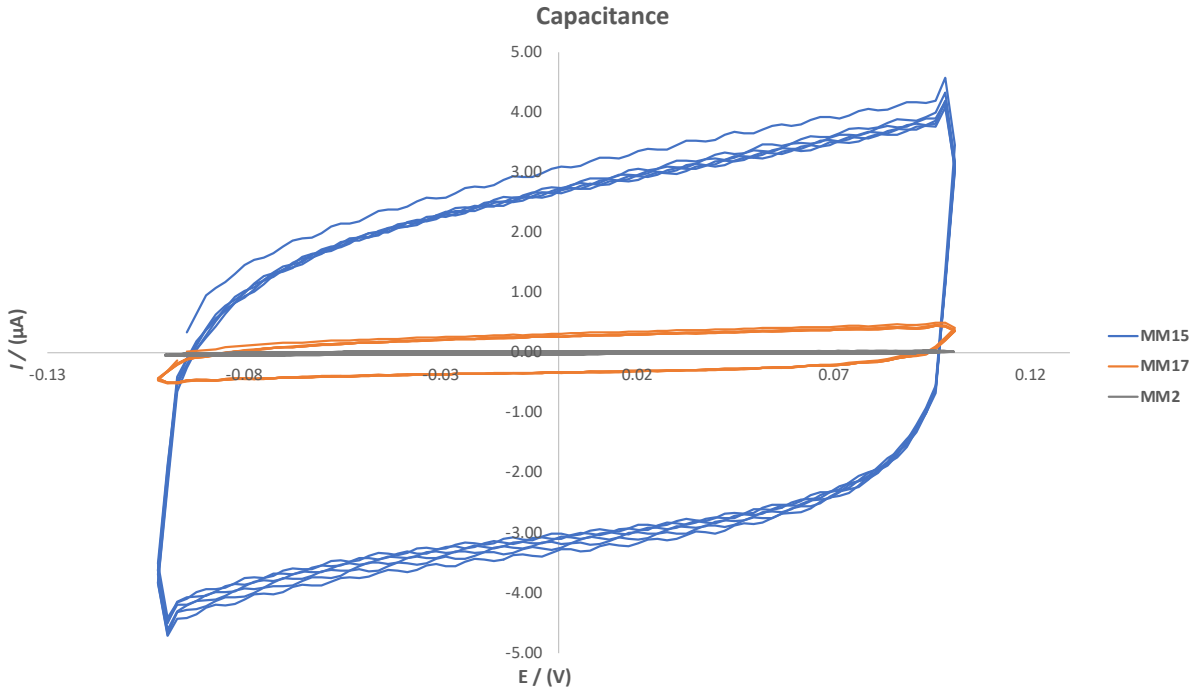

Fig.45 – O-terminated capacitance CVs (v = 50mV/s) in 100mM KNO_3.

The effect of O-termination can be seen immediately on the plot, with current values around 10 times higher for MM15 than the H-terminated electrodes. The effect of O-termination on MM17 is much less significant, with current values roughly doubling.

Capacitance values were calculated and are shown in Table 11.

Table 11 - Capacitance values for O-terminated MM15 and MM17.

Electrode	Capacitance / (μF cm^{-2})
MM2 (Flat)	6.3
MM15	828.0
MM17	84.7

The effect on the capacitance value of MM15 after O-termination is large, as it has increased by ~14 times. The capacitance of MM17 has roughly doubled. However, both have significantly higher capacitance values than a conventional flat electrode (MM2).

Comparing the results to those achieved by May *et al*.[30] (Table 1), their data suggests that capacitance is proportional to bSi needle length. The needle lengths of MM15 and MM17 are ~3.5μm. This means they are longer than the short (~1μm) bSi needles used by May *et al*., but shorter than the long (~15 - 20μm) needles. Therefore, the capacitance values should lie somewhere in between those obtained for the short-bSi needles and the long-bSi needles.

The capacitance of MM17 (84.7 μF cm^{-2}) is larger than the short BDD-coated bSi short needles, but still significantly lower than the BDD-coated bSi long needles. This is concurrent with the data in Table 1.

However, the capacitance calculated for MM15 (828.0 μF cm^{-2}) is very high, larger than any of the capacitance values for the electrodes produced by May *et al*.[30] under the same conditions. This could be due to electrolyte solution leaking underneath the Teflon tape used to define the 3mm diameter geometrical area. This would mean more BDD is exposed to the electrolyte, hence increasing the measured current and therefore the capacitance, as can be seen in Eqn.5.

Alternatively, the disparity in capacitance values between MM15 and MM17 could be due to surface characterisation differences. The deposition of the BDD film upon the bSi substrate in MM17, seen in the SEM images (Figs.42 and 43), is noticeably scarcer than for MM15 (Figs.40 and 41). MM17 resembles the bSi structure, and significantly less diamond growth can be seen along the needles, leading to lower capacitance values.

Capacitance measurements will need to be repeated with a new electrode synthesised in the same way as MM15. This will confirm whether the unusually high capacitance value is due to leakage of electrolyte solution or differences in surface characterisation.

Further Electrochemical Analysis

Next, a 100cm^3 1mM $K_3[Fe(CN)_6]$ solution with 100mM KCl was produced and poured into a three-electrode glass cell as before. A graphite counter and an Ag/AgCl reference electrode were used. Various scans were produced for MM2, MM15 and MM17 at different scan rates, in the potential range 0V to 0.4V. Fig.46 shows the CV for MM15, while the CVs for MM2 and MM17 (Figs.46a and 46b) can be found in Section 1 of the appendix.

The plots all show the characteristic ‘duck-shape’, indicative of oxidation and reduction peaks. This shows that all three samples had been successfully made into functioning electrodes. The scan at 75mV/s for MM2 produced an anomalous result, as can be seen on Fig.46a. This would simply need to be repeated, as the other scans follow a consistent pattern.

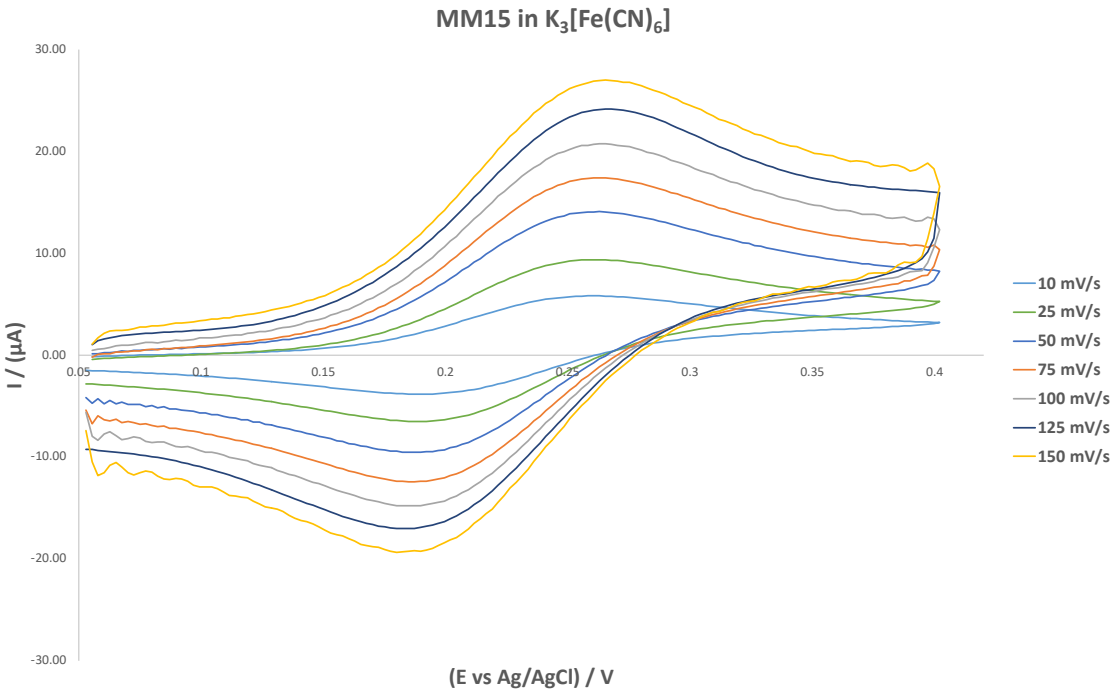

Fig.46 - CV plots for MM15 in 1mM $K_3[Fe(CN)_6]$ with 100mM KCl, at a variety of scan rates.

May *et al.*[30] have also produced current density plots for each electrode at 50mV/s, as well as a plot for an electrode at a variety of scan rates. These are shown in Fig.47.

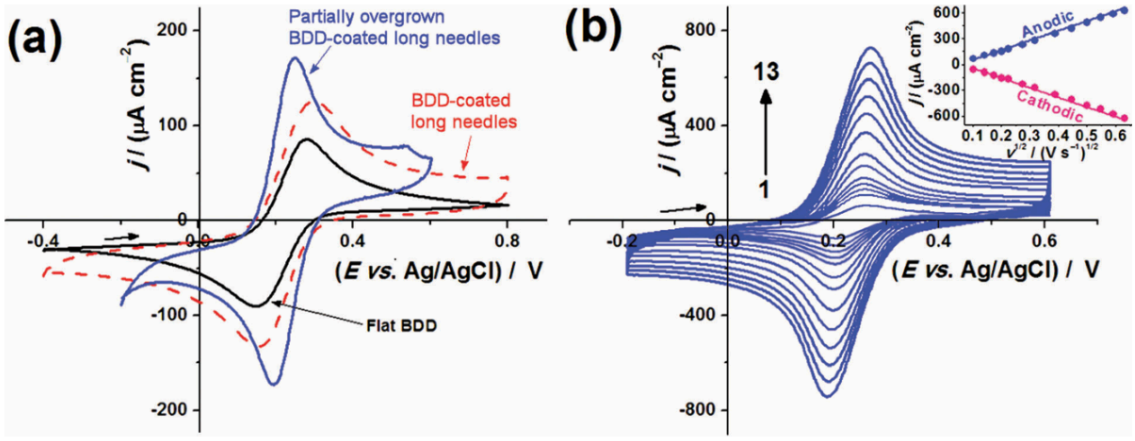

Fig.47 – Current density plots for a) flat-BDD, BDD-coated long and BDD-coated overgrown needles at 50mV/s. b) Current density plots for partially overgrown BDD-long needles at a variety of scan rates. Taken from Ref.030.

Fig.48 shows the current density plot for MM15 at a variety of scan rates (10mV/s to 150mV/s). Current density plots for MM2 and MM17 at the same scan rates can be found in Section 2 of the appendix (Figs.48a and 48b).

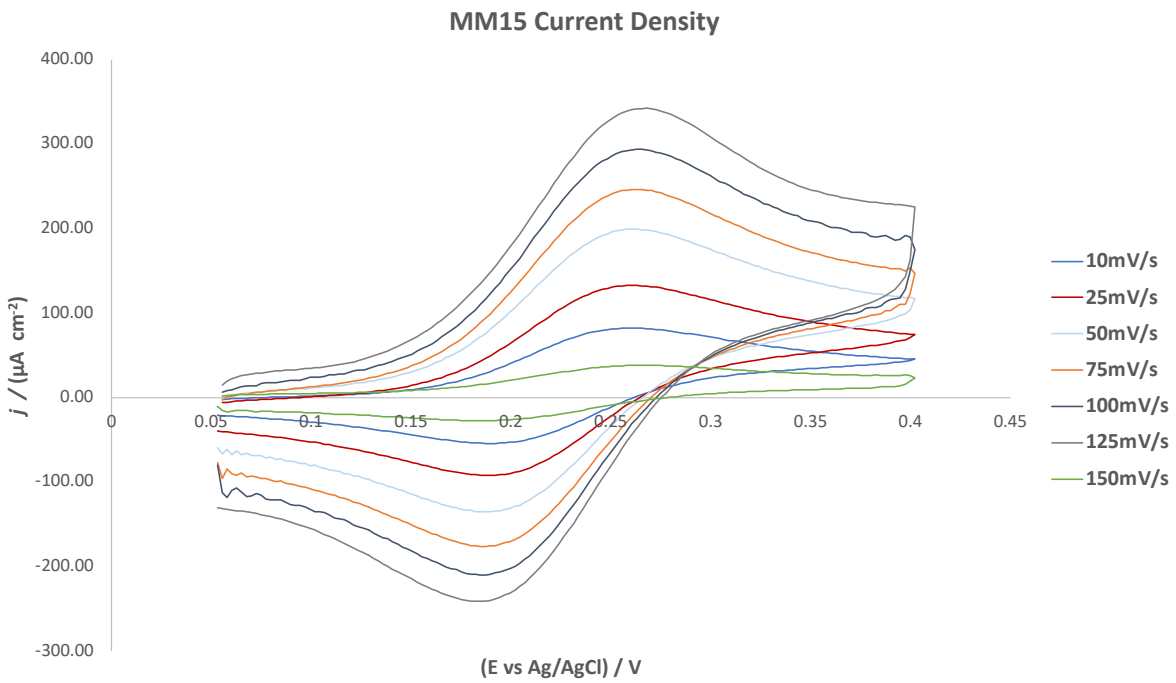

Fig.48 – Current density plots for MM15 in 1mM $K_3[Fe(CN)_6]$ with 100mM KCl, at a variety of scan rates.

Fig.49 shows the current density plots for MM2, MM15 and MM17 at a scan rate of 50mV/s.

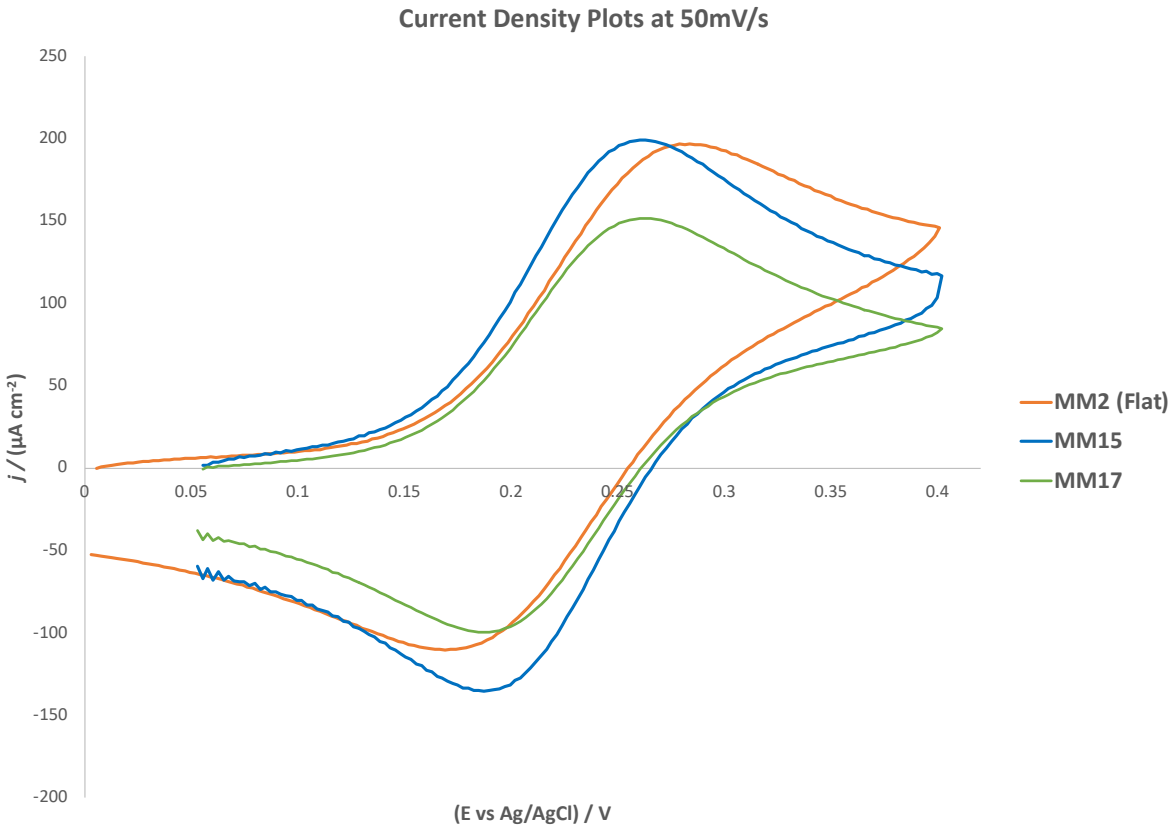

Fig.49 – Current density plots for MM2, MM15 and MM17 in 1mM $K_3[Fe(CN)_6]$ with 100mM KCl, at 50mV/s

The current density plot for the flat MM2 electrode looks very similar to the nanostructured electrodes, MM15 and MM17. This is unusual, especially compared to MM15, as the capacitance value was ~138 times greater than MM2. The reason for this was discussed with A.Black, although no explanation could be made. It is thought that there are problems with MM2, as it was a previously synthesised electrode. A new flat diamond sample was needed; however this was not fabricated before the end of this work.

Positively, the current density plots for MM15 and MM17 are similar to those produced by May *et al*.[30] The maximum current density that May *et al*. measured was ~ 170 μA cm^{-2} for the partially-overgrown long bSi needles. This is compared to ~ 200 μA cm^{-2} for MM15.

Determination of the Surface Area of bDi Electrodes

It is noted by Macpherson[40] that it becomes difficult to accurately measure the surface area of the electrode as the surface becomes rougher. May *et al.*[30] assume that the geometric and effective surface area for the flat diamond electrode was roughly equal. The surface areas of the nanostructured electrodes were then calculated from the ratio of the capacitances. Table 12 shows the relative effective surface areas using this method.

Table 12 - Relative effective surface area values calculated using capacitance ratios.

Electrode	Capacitance / (μF cm^{-2})	Relative Effective Surface Area (Capacitance Ratio)
MM2	6.3	1
MM15	828.0	132
MM17	84.7	13.5

Another method to calculate the electroactive surface area of MM15 and MM17 is to manually measure the needle lengths using the SEM images. However, a number of assumptions were made.

1. The needles are cylinders.
2. The tops of the needles are flat.
3. The bottom of the surface is completely covered by needles (so that diamond deposition on the bottom of the substrate can be ignored) .
4. All needles within the electroactive surface area are identical.

MM15 was calculated first. From Figs.40 and 41, the needle lengths of MM15 are ~3.5μm. This means they are longer than the short (~1μm) bSi needles used by May *et al*.[30], but shorter than the long (~15 - 20μm) needles.

The tops of the needles were measured to have a diameter of ~0.4μm, meaning there are ~2 x 10^6 needles within the exposed 3mm area. The surface area of each needle was calculated to be ~4.53$μm^2$, giving an electroactive surface area of ~0.8cm^2. This makes the electroactive surface area of MM15 ~12 times greater than the flat electrode (MM2). The process was repeated for MM17, with the surface area value being almost identical.

In Table 1, May *et al*.[30] report that the effective surface area of the BDD-coated short bDi needles is 2.6 times greater than the flat diamond electrode. They also report that the effective surface area of the BDD-coated long bSi needles is 97 times greater than the flat diamond electrode.

The needle length in MM15 and MM17 is ~3.5μm, ~3.5 times longer than the short bSi needles used by May *et al*.[30], and ~5 times shorter than the long bSi needles. An effective surface area value of ~12

times greater than the flat electrode for MM15 and MM17 is concurrent with their data, despite the assumptions made in the calculations. These assumptions lead to an underestimate of the surface area, as they do not account for electroactive BDD along the bottom of the substrate. Table 12 shows the full capacitance and effective surface area results.

Table 13 - Final capacitance and effective surface area values for all electrodes.

Electrode	Capacitance / (μF cm^{-2})	Relative Effective Surface Area (Capacitance Ratio)	Relative Effective Surface Area (From SEM Images)
MM2	6.3	1	1
MM15	828.0	132	12
MM17	84.7	13.5	12

These results confirm that MM15 has an effective surface area much greater than expected within a 3mm diameter geometric surface area. The relative surface areas calculated for MM17 are roughly equal; this should also be the case for MM15. However, due to the unusually high capacitance value, it is likely that more of the electrode than the 3mm diameter area are exposed to electrolyte solution.

Conclusions

An ideal electrode material should be chemically inert and highly conductive, as well as having a high surface area. The ability to dope carbon with boron during the CVD process allows highly conducting thin diamond films to be produced. These films are mechanically hard, chemically stable, and can be deposited onto nanostructured substrates to produce high surface area electrodes. bSi is an excellent candidate for a high surface area substrate, due to the nanoscale spikes and needles along its surface. Depositing CVD BDD films on a bSi substrate has been shown to produce functioning electrodes, with properties that are ideal for electrochemical applications. Previous research has seen applications of these electrodes in water treatment and hormone detection.

In this work, both flat (MM2) and bSi (MM15 and MM17) electrodes were produced. Initially, the set of conditions used for the seeding (3hrs seeding, 1hr drying at 50°C) and subsequent growth of the BDD film on the bSi substrate were not optimal as solid build up on the surface could be seen. This was confirmed by SEM imaging. Two new seeding methods (MM15: 3hrs seeding, 1.5hrs drying at 30°C; MM17: 3hrs seeding, 2hrs drying in air) were tested. SEM imaging (Figs.40, 41) confirmed that MM15 had seen more successful diamond growth along the length of the bSi needles. Whilst MM17 was successful, there was visibly less diamond growth on the SEM images (Figs.42, 43) along the length of the bSi needles.

The BDD film was initially H-terminated, which was found to severely limit the electroactive surface area, due to its hydrophobicity. However, capacitance values were obtained (Table 10) which were ~10 times higher than for a conventional flat diamond electrode. Subsequent O-termination of the diamond led to a dramatic increase in capacitance (Table 11) for both MM15 (828 μF cm^{-2}; ~ 14 times increase) and MM17 (84.7μF cm^{-2}; ~ 2 times increase). These were compared to data collected by May *et al*.[30] (Table 1), with the capacitance value for MM15 ~ 30% larger than the largest value obtained in Table 1, for the partially-overgrown long bSi needles.

Calculating the electroactive surface area of an electrode becomes increasingly difficult as the surface becomes rougher.[40] The surface area of MM15 and MM17 was calculated using capacitance ratios, as well as using the SEM images (Figs.40, 41, 42, 43), with a number of assumptions made. Two different values for the geometric surface area were calculated for MM15, suggesting that there was leakage of electrolyte solution outside of the geometric surface area of the electrode. From the SEM images, MM15 and MM17 have surface areas ~ 12 times larger than a flat electrode, with this value

being an underestimate due to BDD deposition along the surface of the substrate not being considered. This value is concurrent with the data obtained in Table 1 by May *et al*.[30], as the bSi needle length used in this work was ~3.5μm.

Future Work

In future, a new flat O-terminated BDD electrode needs to be synthesised, as the current density plot (Fig.49) for MM2 is unusual.

Additionally, the data in Table 1 suggests that capacitance is proportional to bSi needle length. This makes the capacitance for MM15 (828 μF cm^{-2}) unusual. This could be due to electrolyte solution leaking outside of the 3mm diameter area defined by the Teflon tape, which would hence increase the current and therefore the capacitance, as can be seen in Eqn.5. Synthesising a new bSi BDD electrode with the same conditions and needle length as MM15 should be undertaken.

Furthermore, the possibility of electrolyte solution leaking to undesired parts of the electrode suggests that a more secure process for preparing bDi electrodes needs to be designed, as this has the potential to significantly affect electrochemical calculations. Additionally, the silver paint connection between the wire and the BDD surface is not particularly strong. A new method would need to be designed for applications where robustness of the electrode is key.

Appendix

Section 1 – Capacitance plots for MM2 and MM17

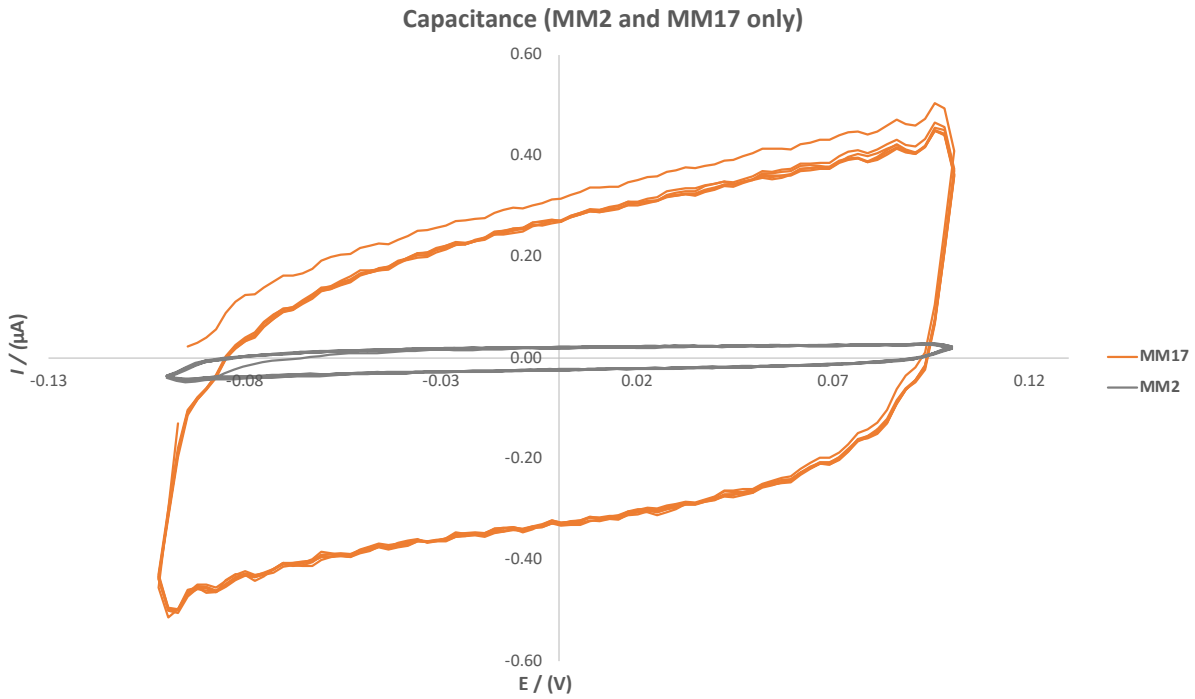

Fig.45a – O-terminated capacitance CVs (v = 50mV/s) in 100mM KNO_3 (MM2 and MM17 only).

Section 2 – CV plots in 1mM $K_3[Fe(CN)_6]$ with 100mM KCl, at a variety of scan rates.

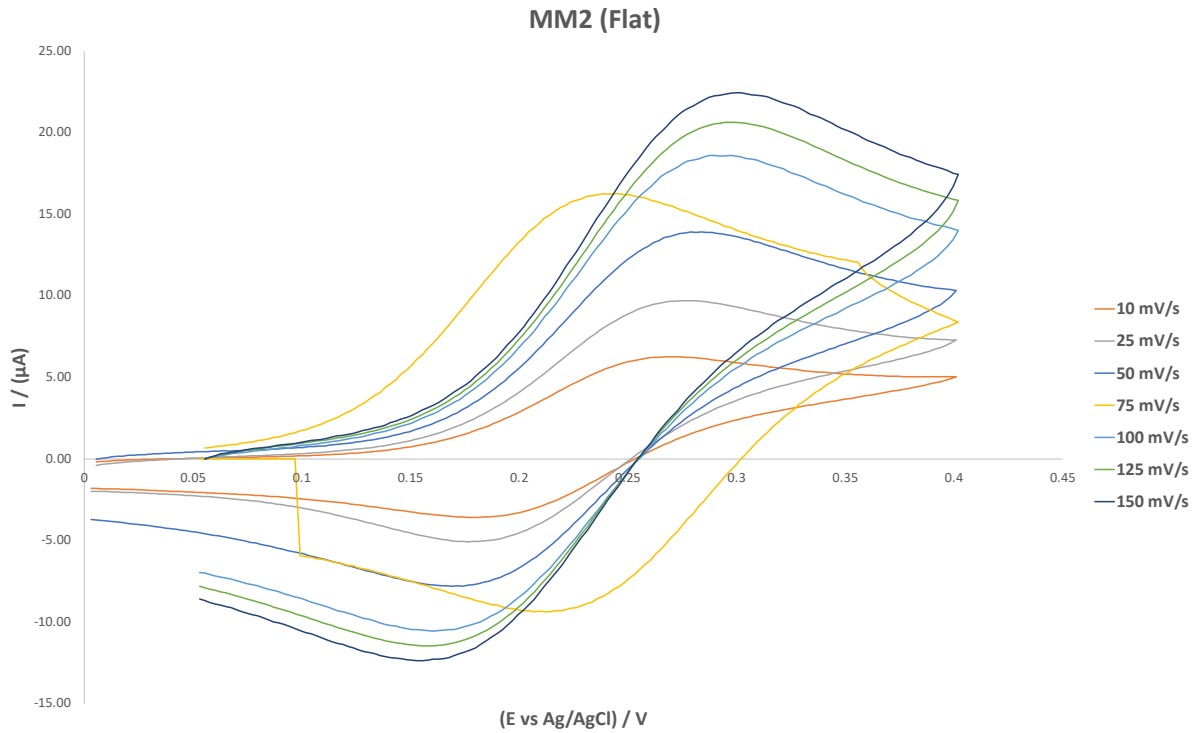

Fig.46a - CV plots for MM2 (flat) in 1mM $K_3[Fe(CN)_6]$ with 100mM KCl, at a variety of scan rates.

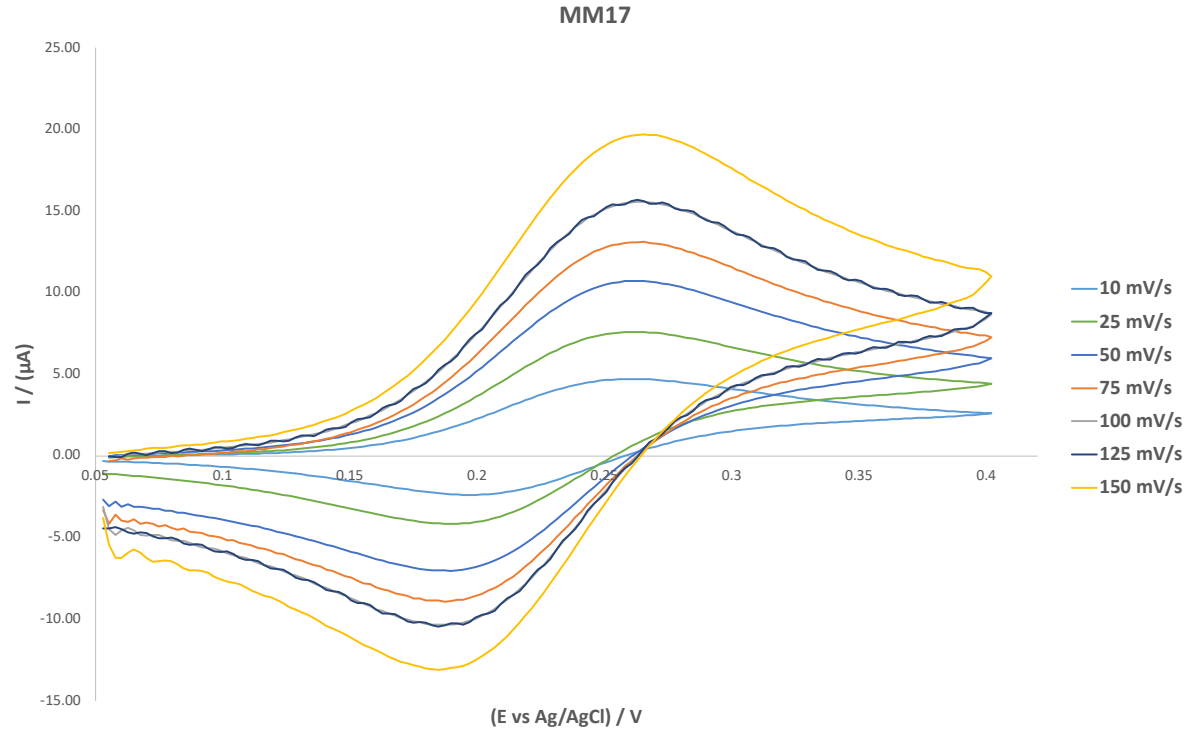

Fig.46b - CV plots for MM17 in 1mM $K_3[Fe(CN)_6]$ with 100mM KCl, at a variety of scan rates.

Section 3 – Current density plots in 1mM $K_3[Fe(CN)_6]$ with 100mM KCl, at a variety of scan rates.

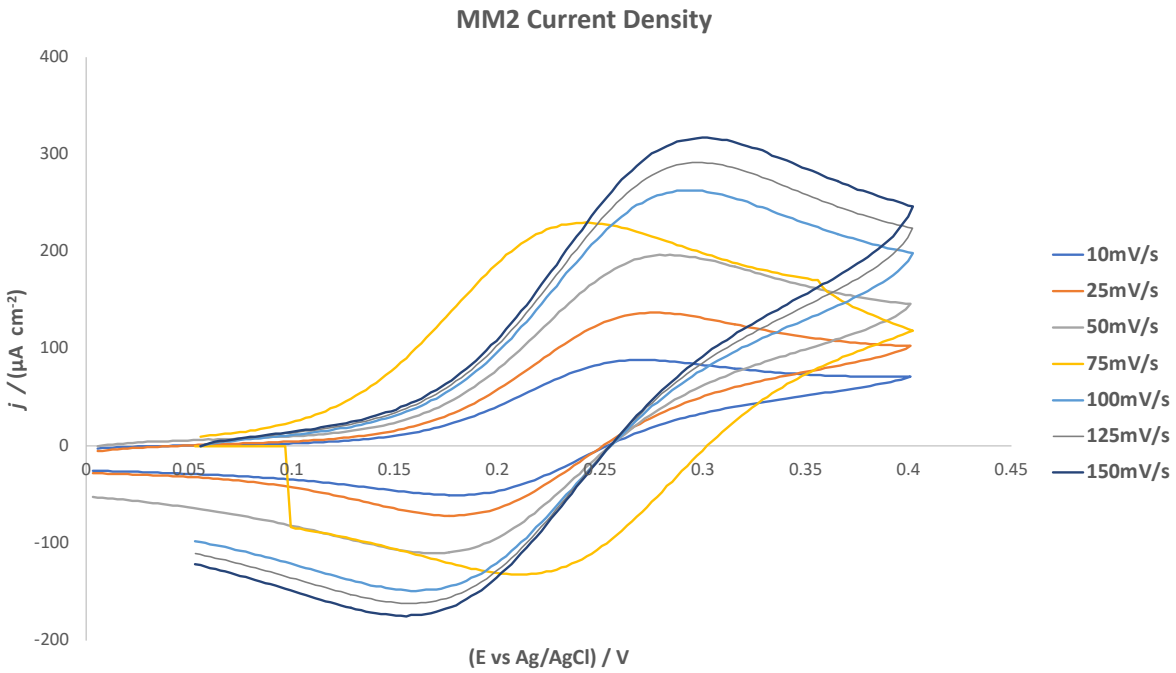

Fig.48a – Current density plots for MM2 in 1mM $K_3[Fe(CN)_6]$ with 100mM KCl, at a variety of scan rates.

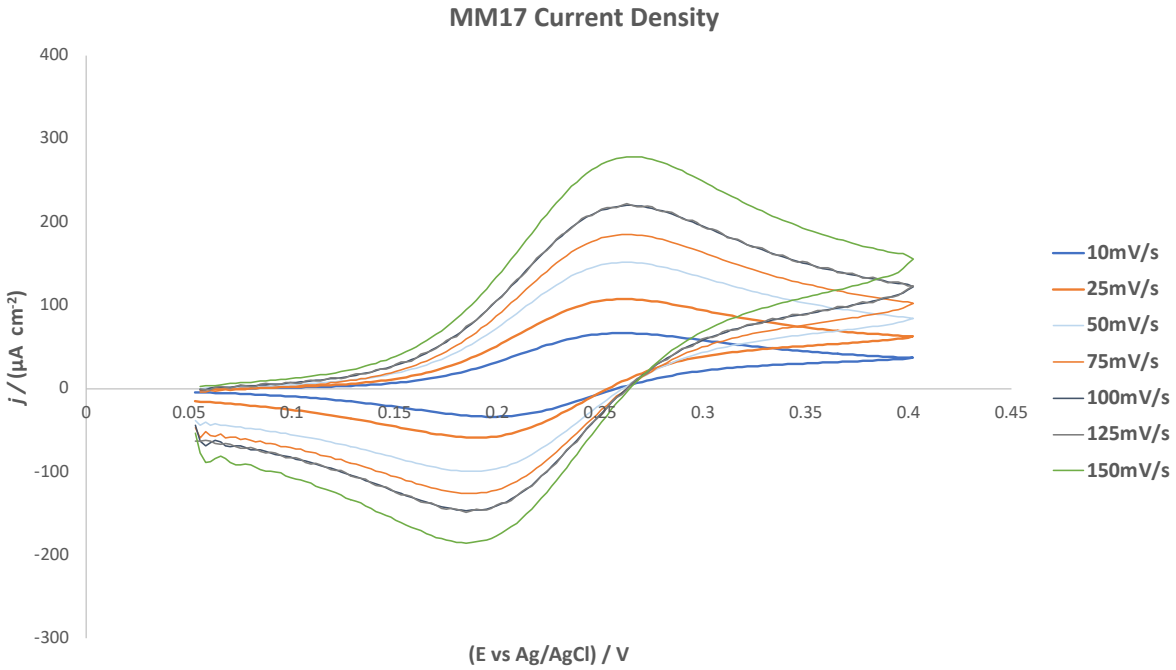

Fig.48b – Current density plots for MM17 in 1mM $K_3[Fe(CN)_6]$ with 100mM KCl, at a variety of scan rates.

References

1- Electrochemistry, https://www.sciencedirect.com/topics/chemistry/electrochemistry, (Accessed 24/12/2022).
2- C.Schotten *et al*., Making electrochemistry easily accessible to the synthetic chemist, *Green Chem*, 2020, **22**, 3358-3375.
3- S.Muhammad, U.Banin Zahra, A.Ahmad, L.Ali Shah, A.Muhammad, Understanding the Basics of Electron Transfer and Cyclic Voltammetry of Potassium Ferricyanide – An Outer Sphere Heterogenous Electrode Reaction, *J. Chem. Soc. Pak*., 2020, **42**, 813-817.
4- R. Douthwaite, Inorganic Mechanisms II, https://www.york.ac.uk/media/chemistry/research/douthwaite/inorganic%20mechanisms%20II.pdf, (Accessed 29/12/2022).
5- Cyclic Voltammetry Basic Principles, Theory and Setup, https://www.ossila.com/pages/cyclic-voltammetry#cyclic-voltammograms, (Accessed 24/12/2022).
6- P.W.May, H. Zanin, D. J. Fermin, D. Plana, S.M.C.Vieira, W.I.Milne and E.J.Corat, Porous Boron-Doped Diamond/Carbon Nanotube Electrodes, *ACS Applied Materials and Interfaces,* 2014, **6**, 990-995.
7- B.Venton, D. DiScenza, *Electrochemistry for Bioanalysis*, Elsevier, University of Virginia, 2020.
8- P.Leung, J.Pijpers, C.León, Optimization in Redox Flow Batteries, *Encyclopaedia of Energy Storage*, 2022, **1**, 545-555.
9- M.Sumantaray, A.Mondal, P.Sudhagar, S.Das, R.Bahru, M.Mohammed, Synergetic Effects of Hybrid Carbon Nanostructured Counter Electrodes for Dye-Sensitized Solar Cells: A Review, *Materials*, 2020, **13**, 2779.
10- E.Frackowiak, F.Beguin, Carbon Materials for the Electrochemical Storage of Energy in Capacitors, *Carbon*, 2001, **39 (6)**, 937-950.
11- A.Agrawal, S.Janakiraman, K.Biswas, A.Venimadhav, S.K.Srivastava, S.Ghosh, Understanding the improved electrochemical performance of nitrogen-doped hard carbons as an anode for sodium ion battery, *Electrochimica Acta*, 2019, **317**, 164-172.
12- R.Schnupp, R.Kühnhold, G.Temmel, E.Burte, H.Ryssel, Thin carbon films as electrodes for bioelectronic applications, *Biosensors and Bioelectronics*, 1998, **13 (7–8)**, 889-894.
13- Chemical Vapour Deposition, https://www.sciencedirect.com/topics/materials-science/chemical-vapor-deposition, (Accessed 12/12/2022)
14- Lab-Grown Diamonds I: Why They Outshine the Conventional Gem, https://muegge.de/en/lab-grown-diamonds-1-why-they-outshine-the-conventional-gem/, (Accessed 24/12/2022).
15- V.Taillandier, High speed imaging detectors with diamond dynode materials, 2013.
16- P.W.May, Diamond thin films: a 21st-century material, *Phil. Trans. R. Soc. A,* 2000, **358,** 473–495.
17- Understanding the difference between n- and p-type semiconductors, https://www.power-and-beyond.com/understanding-the-difference-between-n-and-p-type-semiconductors-a-905805/, (Accessed 24/12/2022).
18- Conduction Band, https://energyeducation.ca/encyclopedia/Conduction_band, (Accessed 12/12/2022).
19- Conduction and Valence Band in Semiconductors, https://www.nuclear-power.com/nuclear-engineering/radiation-detection/semiconductor-detectors/what-are-semiconductors-properties-of-semiconductors/conduction-and-valence-band-in-semiconductors/, (Accessed 12/12/2022).

20- A.Croot, Boron and nitrogen in diamond: an ab initio simulation, plasma emission spectroscopy and material deposition & characterisation study, PhD Thesis, University of Bristol, 2008.
21- X.He, J.Lei, Y.Geng, X.Zheng, M.Wu, M.Zheng, Preparation of microporous activated carbon and its electrochemical performance for electric double layer capacitor, *J. Phys. Chem. Solids*, 2009, **70**, 738−744.
22- W.Zhang, Z.Huang, G.Cao, F.Kang, Y.Yang, A novel mesoporous carbon with straight tunnel-like pore structure for high-rate electrochemical capacitors, *J. Power Sources,* 2012, **204**, 230−235.
23- P. Zhu, Y.Zhao, Cyclic voltammetry measurements of electroactive surface area of porous nickel: Peak current and peak charge methods and diffusion layer effect, *Materials Chemistry and Physics*, 2019, **233**, 60–67.
24- I.Cho, D.H.Kim, S.Park, Electrochemical biosensors: perspective on functional nanomaterials for on-site analysis, *Biomater Res*, 2020, **24**, 6.
25- T.Silva, H.Zanin, P.W.May, E.Corat, O.Fatibello-Filho, Electrochemical Performance of Porous Diamond-like Carbon Electrodes for Sensing Hormones, Neurotransmitters, and Endocrine Disruptors*, ACS Appl. Mater. Interfaces*, 2014, **6**, 21086−21092.
26- H. Zanin, P.W. May, R.L. Harniman, T. Risbridger, E.J. Corat, D.J. Fermin, High surface area diamond-like carbon electrodes grown on vertically aligned carbon nanotubes, *Carbon*, 2015, **82**, 288-296.
27- H.Zanin, P.W.May, A.Lobo, E.Saito, J.Machado, G.Martins, V.Trava-Airoldi, E.Corat, Effect of Multi-Walled Carbon Nanotubes Incorporation on the Structure, Optical and Electrochemical Properties of Diamond-Like Carbon Thin Films, *J. Electrochem. Soc*., 2014, **161 (5)**, H290−H295.
28- H.Zanin, P.W.May, M.Hamanaka, E.Corat, Field Emission from Hybrid Diamond-Like Carbon and Carbon Nanotube Composite Structures, *ACS Appl. Mater. Interfaces*, 2013, **5 (23)**, 12238−12243.
29- A.Sukeri, L.Patricio, H.Saravia, M.Bertotti, A facile electrochemical approach to fabricate a nanoporous gold film electrode and its electrocatalytic activity towards dissolved oxygen reduction, Supporting information, *Physical Chemistry Chemical Physics,* 2015.
30- P. W. May, M. Clegg, T. A. Silva, H. Zanin, O. Fatibello-Filho, V. Celorrio, D. J. Fermin, C. C. Welch, G. Hazell, L. Fisher, A. Nobbs, B. Sue, Diamond-coated 'black silicon' as a promising material for high-surface-area electrochemical electrodes and antibacterial surfaces, *J. Mater. Chem. B*, 2016, **4**, 5737-5746.
31- L. Hutton, M.Vidotti, A. Patel, M. Newton, P. Unwin, J. Macpherson, *J. Phys. Chem*., 2011, **115**, 1649–1658.
32- C. Welch, R. Compton, The use of nanoparticles in electroanalysis: a review, *Anal. Bioanal. Chem*., 2006, **384**, 601.
33- K. E. Bennet, J. R. Tomshine, H-K. Min, F. S. Manciu, M. P. Marsh, S. B. Paek, M. L. Settell, E. N. Nicolai, C. D. Blaha, A. Z. Kouzani, S-Y. Chang, K. H. Lee, A Diamond-Based Electrode for Detection of Neurochemicals in the Human Brain, *Front. Hum. Neurosci.,* 2016, **10**, 1- 12.
34- Deep Brain Stimulation, https://www.mayoclinic.org/tests-procedures/deep-brain-stimulation/about/pac-20384562#dialogId39056175, (Accessed 06/01/2023).
35- M. Bernard, C. Baron, A. Deneuville, About the origin of the low wave number structures of the Raman spectra of heavily boron doped diamond films, *Diam. Relat. Mater.,* 2004, **13**, 896–899.
36- S. Y. Chang, Y. M. Shon, F. Agnesi, K. H. Lee, Microthalamotomy effect during deep brain stimulation: potential involvement of adenosine and glutamate efflux, *Annu Int Conf IEEE Eng Med Biol Soc.* 2009, **2009**, 3294-3297.

37- G. Loos, T. Scheers, K. V. Eyck, A. V. Schepdael, E. Adams, B. V. Bruggen, D. Cabooter, R. Dewil, Electrochemical oxidation of key pharmaceuticals using a boron doped diamond electrode, *Separation and Purification Technology*, 2018, **195**, 184-191.
38- From electrolysis to diamond electrodes, https://www.proaqua.at/en/technologie/, (Accessed 13/01/2023)
39- What is Chemical Oxygen Demand (COD)?, https://www.scimed.co.uk/education/what-is-chemical-oxygen-demand-cod/, (Accessed 13/01/2023).
40- J. Macpherson, A practical guide to using boron doped diamond in electrochemical research, *Phys. Chem. Chem. Phys.*, 2015, **17**, 2935-2949.
41- J. Hansen, R. Copperthwaite, T. Derry, J. Pratt, A tensiometric study of diamond (111) and (110) faces, *J. Colloid and Inter. Sci*., 1989, **130**, 347-358.